Dynamics of boson quantum films

B. E. Clements
Institute Laue Langevin, 38042 Grenoble Cedex, France

H. Forbert
Department of Physics, Texas A&M University, College Station, Texas 77843

E. Krotscheck
Department of Physics, Texas A&M University, College Station, Texas 77843
and Institute for Theoretical Physics, University of California at Santa Barbara, Santa Barbara, California 93106

H. J. Lauter
Institute Laue Langevin, 38042 Grenoble Cedex, France

M. Saarela
Department of Theoretical Physics, University of Oulu, SF-90570 Oulu, Finland

C. J. Tymczak
Department of Physics, Texas A&M University, College Station, Texas 77843
(Received 23 March 1994)

We employ a quantitative microscopic theory of nonuniform quantum liquids to explore the excitations in thin films of ^{4}He adsorbed onto a substrate. These liquid films studied undergo a series of structural phase transitions coinciding with the completion of individual atomic layers. A generalized Feynman ansatz is used for the wave function of the excited states; multiphonon effects are included by generalizing the Feynman theory to allow for time-dependent pair correlations. We study the dispersion relation, excitation mechanisms, transition densities, and particle currents, as a function of the surface coverage, including coverages near the phase transitions. Because of the film's layered growth, the sound velocity exhibits a series of minima and maxima. A pronounced long-wavelength softening of the lowest-energy mode is observed near the transitions. In the monolayer, the nature of the excitations undergoes a noticeable change at the coverage where the velocity of sound starts to *decrease*. This is a crossover from "essentially two-dimensional" to "essentially three-dimensional" behavior. At long wavelengths, below and above the crossover coverage, the lowest-energy excitation is a longitudinal phonon (propagating within the monolayer) and a surface excitation, respectively. At shorter wavelengths, a layer-phonon propagating within the liquid layers, level crosses with a surface excitation to become the lowest-energy mode. For double- and higher-layer films the excitations are complicated by multiple (layer phonon with layer phonon and layer phonon with surface excitation) level crossings. At higher coverages, a mode is identifiable that will evolve into the bulk phonon-maxon roton. Our results agree qualitatively with the available spectra obtained by neutron-scattering experiments.

I. INTRODUCTION

This is the second in a series of papers which is devoted to a microscopic study of the structure, dynamics, and thermodynamics of mono- and multilayer helium films. In a previous paper (Ref. 1, hereafter cited as paper I), we have examined the growth mechanisms, energetics, and the structure of mono-, double-, and triple-layer films. We have shown that the transition between the different structures is *not* a continuous process, but rather occurs in a number of well-defined discrete steps reflecting the formation of individual atomic layers.[1,2] For low-coverage monolayer films, we found that the film is reasonably well described by a two-dimensional model but the agreement between the structure and energetics of the monolayer and the two-dimensional model disappears abruptly at a well-defined crossover coverage; the monolayer starts to display it's three-dimensional nature.

Our specific model under consideration is a layered system of liquid-helium atoms adsorbed to a solid ^{4}He bilayer that is physisorbed to a graphite substrate. The ground-state structure in such systems has been discussed in detail in paper I. The inert substrate and the two layers of solid helium are represented by an external substrate potential $U_{\rm sub}(z)$, which depends on the coordinate z only. As a consequence, the liquid is translation-

ally invariant in the x-y plane and exhibits a "layered" density profile in the z direction. A peculiarity of the liquid film system is that stable, translationally invariant configurations *cannot* be obtained for all surface coverages. Rather, we found in paper I that three "islands" of stable coverages occur in the growth of a triple-layer film. Between the regions of stable coverages, the film passes through a first-order phase transition. Since these transitions occur at the early stage of growth of each layer, we have termed them "layering transitions." A sequence of representative stable density profiles $\rho_1(z)$ of such films is shown in Fig. 1. A similar growth scenario has meanwhile also been found in the path-integral Monte Carlo (PIMC) calculations by Wagner and Ceperley[3] for helium on hydrogen.

Equipped with precise knowledge of the ground-state structure, we proceed in this paper to have a closer look at the nature of the low-lying excited states of the system. As was done in paper I, particular attention will be given to the possible observable consequences of the crossover from an "essentially two-dimensional" to an "essentially three-dimensional" system.

Our paper is organized as follows: In the next section, we will formulate a general theory of excited states which is based on the concept of temporally fluctuating correlation functions. We will derive a set of equations of motion for time-dependent one- and two-body correlations. By including time-dependent two-body correlations we have allowed for multiphonon effects. Multiphonon effects are known to have significant consequences on the zero-sound dispersion relation in bulk liquid ^{4}He; in particular it is necessary to include such effects in order to explain the energetics and density dependence of the collective excitations in the vicinity of the roton minimum.

In the limit that only single-particle functions are allowed to be time dependent, the theory reduces to the generalized Feynman theory of collective excitations. In that case, our approach is conceptually identical to the one used by Chang and Cohen[4] (see also the review by Edwards and Saam, Ref. 5) for nonuniform quantum systems. Input to the theory are the one- and two-body densities obtained from the ground-state calculations. This input is obtained here from our ground-state correlations described in paper I; it could be replaced by results from Monte Carlo calculations of the pair-distribution function if such data should become available with sufficient accuracy.

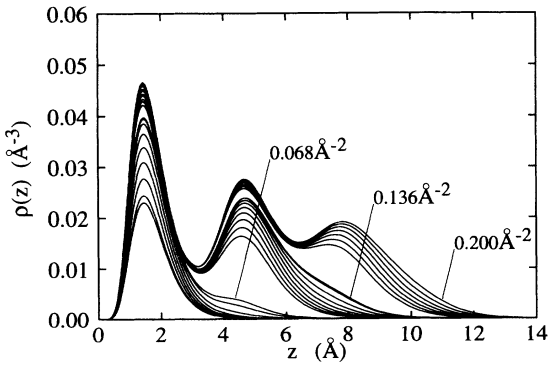

FIG. 1. The density profile of stable configurations of adsorbed films under consideration here. The profiles correspond to surface coverages of 0.033, 0.35, 0.40, ..., 0.065, and 0.068 Å^{-2} for the monolayer, 0.10, 0.105, ..., 0.135, and 0.136 Å^{-2} for the double-layer, and 0.165, 0.170, ..., 0.200 Å^{-2} for the triple layer. The figure is from Ref. 1.

Undoubtedly, the sequence of layering transitions in these systems will have interesting consequences on the excitations. At each spinodal point, where the system becomes unstable against density fluctuations, we expect a "softening" of a collective excitation. The physical nature of the "soft" mode will give information on the type of the phase transition. Furthermore, the mode softening implies an anomalous dispersion at long wavelengths, which in turn allows for the possible decay of a long-wavelength excitation into two excitations. This observation enhances the importance of having a multiphonon theory for film excitations.

Section III is devoted to a systematic study of the low-lying excitations of a liquid monolayer. An indication of the quality of our different approximations used to calculate the excitations is provided by first looking at the limiting cases of two and three dimensions. To achieve an appreciation of the full scope of possible mechanisms in the monolayer, we then study the particle currents and transition densities. Near the low- and high-coverage monolayer instabilities we find an appreciable softening of the lowest mode. We discuss the effect that this softening has on the dynamic structure function.

Multilayer films will be considered in Sec. IV. In these more complicated geometries, we will find a multitude of different excitations corresponding to surface phonons ("ripplons" and/or "third sound") and volume excitations ("bulk phonons") which may be confined to individual liquids layers ("layer phonons").

Section V contains a discussion of the calculation of the dynamic structure function $S(q,\omega)$ on the somewhat simpler level of the Feynman theory for inhomogeneous systems. From the corresponding excitations we calculate $S(q,\omega)$ for mono-, double-, and triple-layer films. We then make a qualitative comparison of our theoretical $S(q,\omega)$ with an experimental one.

II. TIME-DEPENDENT CORRELATIONS

The microscopic description of a strongly interacting system conventionally starts with an empirical Hamiltonian

$$H=\sum_{i=1}^{N}\left\{-\frac{\hbar^2}{2m}\nabla_i^2+U_{\rm sub}(\mathbf{r}_i)\right\}+\sum_{1\le i<j\le N}v(|\mathbf{r}_i-\mathbf{r}_j|), \tag{2.1}$$

where $U_{\rm sub}(\mathbf{r})$ is an external "substrate" potential, and $v(|\mathbf{r}_i-\mathbf{r}_j|)$ is the interaction between individual particles, which we take to be the Aziz potential.[6] The ground-state wave function for a system of N identical bosons with

coordinates $\mathbf{r}_1,\ldots,\mathbf{r}_N$ is approximated by a variational *ansatz*[7] of the form

$$\Psi_0(\mathbf{r}_1,\ldots,\mathbf{r}_N)=\exp\frac{1}{2}\left\{\sum_i u_1(\mathbf{r}_i)+\sum_{i<j}u_2(\mathbf{r}_i,\mathbf{r}_j)+\sum_{i<j<k}u_3(\mathbf{r}_i,\mathbf{r}_j,\mathbf{r}_k)+\cdots\right\}. \tag{2.2}$$

The one-body function $u_1(\mathbf{r})$ describes the spatial structure of the system, and the two-body function $u_2(\mathbf{r}_i,\mathbf{r}_j)$ describes the short- and long-range correlations between pairs of particles. Triplet correlations are needed to provide quantitative agreement between theoretical predictions and the experimental equation of state,[8–10] they also contribute visibly to the nearest-neighbor peak of the pair-distribution function. The correlation functions $u_n(\mathbf{r},\ldots,\mathbf{r_n})$ are determined by minimization of the energy-expectation value E_0:[11]

$$\frac{\delta E_0}{\delta u_n(\mathbf{r},\ldots,\mathbf{r_n})}=0. \tag{2.3}$$

Central quantities of the theory are n-body densities

$$\rho_n(\mathbf{r}_1,\ldots,\mathbf{r}_n)=\frac{N!}{(N-n)!}\frac{\int d^3r_{n+1}\cdots d^3r_N\Psi_0^2(\mathbf{r}_1,\ldots,\mathbf{r}_N)}{\int d^3r_1\cdots d^3r_N\Psi_0^2(\mathbf{r}_1,\ldots,\mathbf{r}_N)} \tag{2.4}$$

and the two-body distribution function

$$g(\mathbf{r}_1,\mathbf{r}_2)=\frac{\rho_2(\mathbf{r}_1,\mathbf{r}_2)}{\rho_1(\mathbf{r}_1)\rho_1(\mathbf{r}_2)}. \tag{2.5}$$

Other key ingredients will be introduced as needed.

In the present and the previous work, we have used the optimized hypernetted-chain Euler-Lagrange (HNC/EL) theory for nonuniform quantum liquids[12] to describe the ground-state structure. We have verified in the preceding paper that this theory provides excellent agreement of our ground-state structure with experiments (when available) and Monte Carlo calculations. This gives us confidence that we have the right starting point to study the excitations in liquid multilayers.

The basic idea of our theory of excitations is to allow for *time-dependent* correlations in the variational wave function (2.2). To formulate the theory, we follow the general route outlined by Saarela and co-workers[13–15] and allow for time-dependent one- *and* two-body correlations. The rationale for including time-dependent two-body correlations is that, when the wavelength of an excitation is comparable to the average distance between pairs of particles, the short-range structure of the system should be affected by the excitation. The wave function of an excited state is written as

$$|\Psi(t)\rangle=e^{-iE_0t/\hbar}|\Psi_0(t)\rangle,\qquad |\Psi_0(t)\rangle=\frac{e^{\frac{1}{2}\delta U(t)}|\Psi_0\rangle}{\left[\langle\Psi_0|e^{\delta U(t)}|\Psi_0\rangle\right]^{1/2}}, \tag{2.6}$$

where $|\Psi_0\rangle$ is the (variational) ground state (2.2), and

$$\delta U=\sum_i\delta u_1(\mathbf{r}_i;t)+\sum_{i<j}\delta u_2(\mathbf{r}_i,\mathbf{r}_j;t) \tag{2.7}$$

is the complex *excitation operator*. The time-dependent correlations are determined by an action principle[16,17]

$$\delta\mathcal{L}=0 \tag{2.8}$$

with a Lagrangian

$$\mathcal{L}=\int dt\left\langle\Psi(t)\left|H-i\hbar\frac{\partial}{\partial t}\right|\Psi(t)\right\rangle=\int dt\left\langle\Psi_0(t)\left|H-E_0-i\hbar\frac{\partial}{\partial t}\right|\Psi_0(t)\right\rangle. \tag{2.9}$$

We can assume that the amplitude of the time-dependent part of the correlations is small such that we can expand the Lagrangian to second order,

$$\mathcal{L}=\int dt\left\{\frac{1}{8}\langle\Psi_0|[\delta U^*,[T,\delta U]]|\Psi_0\rangle-\frac{i\hbar}{8}[\langle\Psi_0|\delta\dot{U}\delta U^*|\Psi_0\rangle-\langle\Psi_0|\delta\dot{U}|\Psi_0\rangle\langle\Psi_0|\delta U^*|\Psi_0\rangle-\text{c.c.}]\right\}. \tag{2.10}$$

For the derivation of the double-commutator term in the above equation, one normally assumes that $|\Psi_0\rangle$ is the exact ground state. However, for the specific form (2.7) of the excitation operator, it is sufficient to assume that the correlations up to u_4 have been optimized. Inserting the explicit form of our time-dependent correlations allows us to rewrite the double-commutator term in terms of one-, two-, and three-body densities:

$$\frac{1}{8}\langle\Psi_0|[\delta U^*,[T,\delta U]]|\Psi_0\rangle=\frac{\hbar^2}{8m}\left\{\int d^3r\rho_1(\mathbf{r})|\nabla\delta u_1(\mathbf{r};t)|^2+\int d^3r_1d^3r_2\rho_2(\mathbf{r}_1,\mathbf{r}_2)\left[\nabla_1\delta u_1(\mathbf{r}_1;t)\cdot\nabla_1\delta u_2^*(\mathbf{r}_1,\mathbf{r}_2;t)+\text{c.c.}+|\nabla_1\delta u_2(\mathbf{r}_1,\mathbf{r}_2;t)|^2\right]+\int d^3r_1d^3r_2d^3r_3\rho_3(\mathbf{r}_1,\mathbf{r}_2,\mathbf{r}_3)\nabla_1\delta u_2(\mathbf{r}_1,\mathbf{r}_2;t)\nabla_1\delta u_2^*(\mathbf{r}_1,\mathbf{r}_3;t)+\text{c.c.}\right\}. \tag{2.11}$$

The time-derivative term in the Lagrangian (2.10) is conveniently expressed in terms of (time derivatives of) the

time-dependent one- and two-body densities $\delta\rho_1(\mathbf{r};t)$ and $\delta\rho_2(\mathbf{r}_i,\mathbf{r}_j;t)$ to be taken to first order in the fluctuations

$$[\langle\Psi_0|\delta\dot{U}\delta U^*|\Psi_0\rangle - \langle\Psi_0|\delta\dot{U}|\Psi_0\rangle\langle\Psi_0|\delta U^*|\Psi_0\rangle] = \int d^3r\dot{\rho}_1(\mathbf{r};t)\delta u_1^*(\mathbf{r};t) + \frac{1}{2}\int d^3r_1 d^3r_2\dot{\rho}_2(\mathbf{r}_1,\mathbf{r}_2;t)\delta u_2^*(\mathbf{r}_1,\mathbf{r}_2;t). \quad (2.12)$$

A word is in order concerning the interpretation of the time derivative of the above densities: These are *not* the time derivatives of the (real) physical density, but rather should be understood as an abbreviation of the operation

$$\dot{\rho}_1(\mathbf{r}_1;t) \equiv \int d^3r_2\left[\frac{\delta\rho_1(\mathbf{r}_1)}{\delta u_1(\mathbf{r}_2)}\right]\delta\dot{u}_1(\mathbf{r}_2;t) + \int d^3r_2 d^3r_3\left[\frac{\delta\rho_1(\mathbf{r}_1)}{\delta u_2(\mathbf{r}_2,\mathbf{r}_3)}\right]\delta\dot{u}_2(\mathbf{r}_2,\mathbf{r}_3;t) \quad (2.13)$$

and a corresponding equation for the time-dependent pair density. In other words, $\dot{\rho}_1(\mathbf{r}_1)$ and $\dot{\rho}_2(\mathbf{r}_1,\mathbf{r}_2)$ are *complex.* The physical time-dependent densities are obtained by taking the real part of these functions.

With this, we have worked out the energy functional to second order in the fluctuations, and can write down the equations of motion.

$$\frac{\hbar^2}{2m}\nabla_1\cdot\left\{\rho_1(\mathbf{r}_1)\nabla_1\delta u_1(\mathbf{r}_1;t) + \int d^3r_2\rho_2(\mathbf{r}_1,\mathbf{r}_2)\nabla_1\delta u_2(\mathbf{r}_1,\mathbf{r}_2;t)\right\} + i\hbar\dot{\rho}_1(\mathbf{r}_1;t) = 0 \quad (2.14)$$

and

$$\frac{\hbar^2}{2m}\nabla_1\cdot\left\{\left[\rho_2(\mathbf{r}_1,\mathbf{r}_2) - \rho_1(\mathbf{r}_1)\rho_1(\mathbf{r}_2)\right]\nabla_1\delta u_1(\mathbf{r}_1;t) + \rho_2(\mathbf{r}_1,\mathbf{r}_2)\nabla_1\delta u_2(\mathbf{r}_2,\mathbf{r}_2;t)\right.$$
$$\left. + \int d^3r_3\left[\rho_3(\mathbf{r}_1,\mathbf{r}_2,\mathbf{r}_3) - \rho_2(\mathbf{r}_1,\mathbf{r}_3)\rho_1(\mathbf{r}_2)\right]\nabla_1\delta u_2(\mathbf{r}_2,\mathbf{r}_3;t)\right\} + \text{ same for } (1\leftrightarrow 2)$$
$$= -i\hbar\left[\dot{\rho}_2(\mathbf{r}_1,\mathbf{r}_2;t) - \rho_1(\mathbf{r}_1)\dot{\rho}_1(\mathbf{r}_2;t) - \dot{\rho}_1(\mathbf{r}_1;t)\rho_1(\mathbf{r}_2)\right]. \quad (2.15)$$

Introducing the one-body current

$$-i\mathbf{j}(\mathbf{r};t) = \frac{\hbar\rho_1(\mathbf{r})}{2m}\left\{\nabla\delta u_1(\mathbf{r};t) + \int d^3r'\rho_1(\mathbf{r}')g(\mathbf{r},\mathbf{r}')\nabla\delta u_2(\mathbf{r},\mathbf{r}';t)\right\}, \quad (2.16)$$

the one-body equation is readily identified with the continuity equation

$$i\hbar\left[\nabla\cdot\mathbf{j}(\mathbf{r};t) - \dot{\rho}_1(\mathbf{r};t)\right] = 0. \quad (2.17)$$

Equations (2.14) and (2.15) are the starting point for the equations-of-motion method for the calculation of collective excitations in quantum liquids. Different implementations[13–15,18,19] differ by the approximations used for the three- and four-body densities appearing in the equations of motion and the time derivative of one- and two-body densities. The most complete evaluation[14,15] of the integral kernels of the equations of motion (2.14) and (2.15) has provided (with an energy of 9.7 K) the best theoretical prediction of the energy of the roton minimum available to date. The simpler convolution approximation,[18] which we shall use here for technical reasons, is not quite as successful, but still bridges a significant portion of the discrepancy between the prediction of the Feynman theory and the experimental roton minimum. We also note that the Feynman-Cohen theory of "backflow[20]" assumes a specific form for $\delta u_2(\mathbf{r},\mathbf{r}';t)$, while in the equation-of-motion method it is solved for.

The original Feynman theory of collective excitations[21] is recovered by omitting the fluctuating pair-correlation function $\delta u_2(\mathbf{r}_i,\mathbf{r}_j;t)$. Our applications for the higher-lying states will partly be based on this approximation and, to the extent that we go beyond that, the "Feynman-phonon" states form a convenient basis to work in. Omitting $\delta u_2(\mathbf{r}_i,\mathbf{r}_j;t)$, we only need to consider the one-body equation (2.14). The time-derivative terms (2.13) reduce to

$$\frac{\delta\rho_1(\mathbf{r}_1)}{\delta u_1(\mathbf{r}_2)} = \rho_1(\mathbf{r}_1)\delta(\mathbf{r}_1-\mathbf{r}_2) + \left[\rho_2(\mathbf{r}_1,\mathbf{r}_2) - \rho_1(\mathbf{r}_1)\rho_1(\mathbf{r}_2)\right]. \quad (2.18)$$

Defining

$$\psi(\mathbf{r}) = \sqrt{\rho_1(\mathbf{r})}\delta u_1(\mathbf{r})e^{i\omega t} \quad (2.19)$$

leads to the generalized eigenvalue problem

$$H_1\psi_n(\mathbf{r}) = \hbar\omega_n\int d^3r' S(\mathbf{r},\mathbf{r}')\psi_n(\mathbf{r}') \quad (2.20)$$

with the coordinate space representation of the static structure function

$$S(\mathbf{r},\mathbf{r}') = \delta(\mathbf{r}-\mathbf{r}') + \sqrt{\rho_1(\mathbf{r})\rho_1(\mathbf{r}')}h(\mathbf{r},\mathbf{r}'), \quad (2.21)$$

where $h(\mathbf{r},\mathbf{r}') \equiv g(\mathbf{r},\mathbf{r}') - 1$, and the kinetic energy operator

$$H_1 = -\frac{\hbar^2}{2m}\frac{1}{\sqrt{\rho_1(\mathbf{r})}}\nabla\rho_1(\mathbf{r})\nabla\frac{1}{\sqrt{\rho_1(\mathbf{r})}}. \tag{2.22}$$

The bulk limit of the eigenvalue problem (2.20) is the well-known Feynman dispersion relation $\omega(k) = \hbar k^2/2mS(k)$. A convenient normalization of the eigenstates of the generalized eigenvalue problem (2.20) is

$$(\psi_m\,|H_1|\,\psi_n) = \hbar\omega_m\delta_{mn}. \tag{2.23}$$

These eigenstates are related to the Feynman excitation functions $\delta u_1(\mathbf{r})$ through Eq. (2.19). The adjoint states

$$\phi_n(\mathbf{r}) \equiv \frac{1}{\hbar\omega_n}H_1\psi_n(\mathbf{r}) \tag{2.24}$$

are related to the physical density fluctuations [cf. Eq. (2.18)],

$$\delta\rho_1(\mathbf{r}) = \sqrt{\rho_1(\mathbf{r})}\phi_n(\mathbf{r}). \tag{2.25}$$

We note in passing that the eigenstates $\phi_n(\mathbf{r})$ and $\psi_n(\mathbf{r})$ are also the essential ingredients of the solution of the Euler equation for the pair correlations and provide a convenient basis for the representation of optimized triplet correlations.[1]

The derivation of workable schemes to solve the time-dependent two-body equation is considerably more complicated than for the generalized Feynman formula (2.20). In particular, a rather elaborate diagrammatic analysis of the three- and four body densities is involved. At the same time, we must keep the numerical feasibility of the theory in mind. We note, first of all, that the two equations of motion (2.14) and (2.15) are *not* independent; the one-body equation follows from the two-body equation in the limit of large distances between the "external" points in the two-body equation, i.e., in the limit $|\mathbf{r}_1 - \mathbf{r}_2| \to \infty$. Moreover, we also recover the one-body equation (2.14) by integrating the two-body equation over one of the external points, say $\mathbf{r}_2$. It is particularly important to maintain this feature in order to guarantee that the theory is qualitatively correct in the long-wavelength limit.

It is beyond the scope of this paper to go through the rather lengthy algebraic derivations; we only sketch the essential steps. To shorten the length of the equations we will drop the explicit time dependence label when it is unambiguous to do so. First, the one- and the two-body equations are decoupled by subtracting the asymptotic limit, multiplied by a pair-distribution function $g(\mathbf{r}_1,\mathbf{r}_2)$. At the same time we rewrite the time derivative of the pair density in terms of the time derivatives of the one-body density and the pair-distribution function. The resulting equation is

$$\frac{\hbar^2}{2m}\nabla_1\rho_1(\mathbf{r}_1)\Big\{g(\mathbf{r}_1,\mathbf{r}_2)\nabla_1\delta u_2(\mathbf{r}_1,\mathbf{r}_2) + \int d^3r_3\rho_1(\mathbf{r}_3)\left[g_3(\mathbf{r}_1,\mathbf{r}_2,\mathbf{r}_3) - g(\mathbf{r}_1,\mathbf{r}_3)g(\mathbf{r}_1,\mathbf{r}_2)\right]\nabla_1\delta u_2(\mathbf{r}_1,\mathbf{r}_3)\Big\}\rho_1(\mathbf{r}_2)$$
$$+ \text{ same for } (1 \leftrightarrow 2)$$
$$= i\hbar\left[\mathbf{j}(\mathbf{r}_1)\cdot\nabla_1 h(\mathbf{r}_1,\mathbf{r}_2)\rho_1(\mathbf{r}_2) + \rho_1(\mathbf{r}_1)\nabla_2 h(\mathbf{r}_1,\mathbf{r}_2)\cdot\mathbf{j}(\mathbf{r}_2)\right] - i\hbar\rho_1(\mathbf{r}_1)\rho_1(\mathbf{r}_2)\dot{g}(\mathbf{r}_1,\mathbf{r}_2). \tag{2.26}$$

The time derivative of the pair-distribution function is then expressed in terms of the time derivative of the *non-nodal* function $X(\mathbf{r}_1,\mathbf{r}_2)$, which are basic components of the HNC scheme, and the one-body density:

$$\dot{g}(\mathbf{r}_1,\mathbf{r}_2) = \int d^3r_3 h(\mathbf{r}_1,\mathbf{r}_3)\dot{\rho}_1(\mathbf{r}_3)h(\mathbf{r}_3,\mathbf{r}_2) + \int d^3r_3 d^3r_4[\delta(\mathbf{r}_1-\mathbf{r}_3) + h(\mathbf{r}_1,\mathbf{r}_3)\rho_1(\mathbf{r}_3)]$$
$$\times\left[\dot{X}(\mathbf{r}_3,\mathbf{r}_4) + \int d^3r_5 X_3(\mathbf{r}_3,\mathbf{r}_4,\mathbf{r}_5)\dot{\rho}(\mathbf{r}_5)\right][\delta(\mathbf{r}_4-\mathbf{r}_2) + \rho_1(\mathbf{r}_4)h(\mathbf{r}_4,\mathbf{r}_2)], \tag{2.27}$$

where $X_3(\mathbf{r}_3,\mathbf{r}_4,\mathbf{r}_5)$ is the set of all three-body diagrams that are non-nodal in all three external points.[22] The final steps of the derivation are the approximations necessary to bring the two-body equation in a numerically tractable form. Our scheme follows the general strategy of the "uniform limit" approximation[7] which has been quite successful for the calculation of the optimal *static* three-body correlations.[8–10] The essence of the approximation is to consider all products of two or more two-body functions small *in coordinate space*. In our specific case, the uniform limit approximation amounts to taking $g(\mathbf{r}_1,\mathbf{r}_2)\delta u_2(\mathbf{r}_1,\mathbf{r}_2) \approx \delta u_2(\mathbf{r}_1,\mathbf{r}_2)$ and a similar expression for $\nabla_1 u_2(\mathbf{r}_1,\mathbf{r}_2)$. While this approximation places more emphasis on the structure of $\delta u_2(\mathbf{r}_1,\mathbf{r}_2)$, it is physically appealing since it simply removes the *redundant* relevant short-range structure shared by $g(\mathbf{r}_1,\mathbf{r}_2)$ and $\delta u_2(\mathbf{r}_1,\mathbf{r}_2)$. Invoking the equivalent uniform limit for the three-body distribution function, the left-hand side of the two-body equation becomes

$$\frac{\hbar^2}{2m}\nabla_1\Big\{\rho_1(\mathbf{r}_1)\Big[g(\mathbf{r}_1,\mathbf{r}_2)\nabla_1\delta u_2(\mathbf{r}_1,\mathbf{r}_2) + \int d^3r_3\rho_1(\mathbf{r}_3)\left[g_3(\mathbf{r}_1,\mathbf{r}_2,\mathbf{r}_3) - g(\mathbf{r}_1,\mathbf{r}_3)g(\mathbf{r}_1,\mathbf{r}_2)\right]\nabla_1\delta u_2(\mathbf{r}_1,\mathbf{r}_3)\Big]\Big\}$$
$$\approx \frac{\hbar^2}{2m}\nabla_1\Big\{\rho_1(\mathbf{r}_1)\nabla_1\int d^3r_3\delta u_2(\mathbf{r}_1,\mathbf{r}_3)\left[\delta(\mathbf{r}_3-\mathbf{r}_2) + \rho_1(\mathbf{r}_3)h(\mathbf{r}_3,\mathbf{r}_2)\right]\Big\}. \tag{2.28}$$

A convenient notation for the convolution product of a pair of two-point functions $A(\mathbf{r}_1,\mathbf{r}_2)$ and $B(\mathbf{r}_1,\mathbf{r}_2)$ is

$$[A*B](\mathbf{r}_1,\mathbf{r}_2)=\int d^3r_3 A(\mathbf{r}_1,\mathbf{r}_3)B(\mathbf{r}_3,\mathbf{r}_2). \tag{2.29}$$

Using the one-body equation to eliminate the time derivative of the density, the two-body equation can be written in the compact form

$$\left[i\hbar\frac{\partial}{\partial t}\delta\tilde{u}_2 - S^{-1}*H_1*\delta\tilde{u}_2 - \delta\tilde{u}_2*H_1*S^{-1}\right](\mathbf{r}_1,\mathbf{r}_2)=i\hbar\Big\{\tilde{\mathbf{j}}(\mathbf{r}_1)\cdot\nabla_1 X(\mathbf{r}_1,\mathbf{r}_2)\sqrt{\rho_1(\mathbf{r}_2)}+\tilde{\mathbf{j}}(\mathbf{r}_2)\cdot\nabla_2 X(\mathbf{r}_1,\mathbf{r}_2)\sqrt{\rho_1(\mathbf{r}_1)}$$

$$-\int d^3r_3\tilde{X}_3(\mathbf{r}_1,\mathbf{r}_2,\mathbf{r}_3)\sqrt{\rho_1(\mathbf{r}_3)}\nabla_3\cdot\mathbf{j}(\mathbf{r}_3)\Big\}. \tag{2.30}$$

In the above equation, we have introduced the following tilde notation $\delta\tilde{u}_2(\mathbf{r}_1,\mathbf{r}_2)\equiv\sqrt{\rho_1(\mathbf{r}_1)}\delta u_2(\mathbf{r}_1,\mathbf{r}_2)\sqrt{\rho_1(\mathbf{r}_2)}$, $\tilde{\mathbf{j}}(\mathbf{r})\equiv\mathbf{j}(\mathbf{r})/\sqrt{\rho_1(\mathbf{r})}$, and the inverse of the static structure function is to be understood in the sense of the convolution product (2.29). The fully irreducible three-body function $\tilde{X}_3(\mathbf{r}_1,\mathbf{r}_2,\mathbf{r}_3)$ is a ground-state quantity; it follows from the solution of the three-body Euler equation. With $\tilde{X}_3(\mathbf{r}_1,\mathbf{r}_2,\mathbf{r}_3)\approx\tilde{u}_3(\mathbf{r}_1,\mathbf{r}_2,\mathbf{r}_3)$, an explicit expression for the latter quantity is given in Eqs. (A23)–(A26) of paper I. Approximating now the full current (2.16) by the Feynman current $\mathbf{j}(\mathbf{r})=(i\hbar/2m)\rho_1(\mathbf{r})\nabla\delta u_1(\mathbf{r})$ allows us to decouple the equations of motion, in other words the fluctuating two-point function can be expressed, in closed form, as a functional of a one-body quantity by inverting the operator on the left-hand side of Eq. (2.30). This inversion can be carried out algebraically in the basis of the Feynman states. For example, the time-dependent part of the density is expanded in terms of the Feynman density fluctuations as

$$\delta\rho_1(\mathbf{r})=\sqrt{\rho_1(\mathbf{r})}\sum_n\varphi_n\phi_n(\mathbf{r}). \tag{2.31}$$

These manipulations allow one to solve the two-body equation explicitly for $\delta u_2(\mathbf{r}_1,\mathbf{r}_2)$. The result is used in the one-body equation (2.14) and yields a nonlinear eigenvalue problem

$$\hbar\omega_s\varphi_s-\frac{1}{2}\sum_{mnt}\frac{V^s_{mn}V^t_{mn}}{\hbar(\omega_m+\omega_n-\omega)}\varphi_t=\hbar\omega\varphi_s. \tag{2.32}$$

Equation (2.32) has the structure that would be predicted, in a weakly interacting system, by Brillouin-Wigner perturbation theory. Of course, all the ingredients of the theory are highly correlated basis states—we will therefore refer to the theory as a correlated basis states-Brillouin-Wigner (CBF-BW) theory. The three-phonon vertices V^s_{mn} are expressed as three-phonon matrix elements

$$V^t_{mn}=-\frac{\hbar^2}{2m}\int d^3r\nabla\left[\frac{\psi_t(\mathbf{r})}{\sqrt{\rho_1(\mathbf{r})}}\right]\cdot\Big\{\xi_m(\mathbf{r})\nabla\zeta_n(\mathbf{r})+(m\leftrightarrow n)\Big\}-\hbar\omega_t X_{mnt}, \tag{2.33}$$

where we have abbreviated, as in paper I

$$\xi_m(\mathbf{r})\equiv\sqrt{\rho_1(\mathbf{r})}\phi_m(\mathbf{r}),\qquad \zeta_m(\mathbf{r})\equiv\frac{\phi_m(\mathbf{r})-\psi_m(\mathbf{r})}{\sqrt{\rho_1(\mathbf{r})}}, \tag{2.34}$$

and X_{mnt} is the matrix element of the ground-state three-body correlation vertex of paper I. Inserting the bulk limits in a normalization volume Ω

$$\psi_m(\mathbf{r})=\frac{1}{\sqrt{S(q_m)}}\frac{e^{i\mathbf{q}_m\cdot\mathbf{r}}}{\sqrt{\Omega}},\qquad \phi_m(\mathbf{r})=\sqrt{S(q_m)}\frac{e^{i\mathbf{q}_m\cdot\mathbf{r}}}{\sqrt{\Omega}}, \tag{2.35}$$

one can, after some straightforward algebra, recover the working formulas of Chang and Campbell.[9]

III. MONOLAYER EXCITATIONS

A discussion of the excitation energetics and mechanisms requires the specification of the geometry. As in our previous work, we assume that the substrate is translationally invariant in the $(x$-$y)$ plane and located at $z<0$. The quantum numbers specifying the states $\psi_n(\mathbf{r})$ and $\phi_n(\mathbf{r})$ are a wave vector $\mathbf{q}_\parallel$ parallel to the surface, and a (discrete or continuous) quantum number describing the z dependence of the excitation functions. Without loss of generality, we can write

$$\psi_n(\mathbf{r})=\frac{1}{L}\psi_{n,\mathbf{q}_\parallel}(z)e^{i\mathbf{q}_\parallel\cdot\mathbf{r}_\parallel},\qquad \phi_n(\mathbf{r})=\frac{1}{L}\phi_{n,\mathbf{q}_\parallel}(z)e^{i\mathbf{q}_\parallel\cdot\mathbf{r}_\parallel}, \tag{3.1}$$

where L is the dimension of the normalization box, and $\mathbf{r}_\parallel$ the coordinate vector parallel to the surface. The

summations over intermediate states in Eq. (2.32) are understood to be summations over the discrete quantum number, and integrals over the parallel momenta. Note that the generalized eigenvalue equation (2.32) decouples in the wave number associated with the amplitudes φ_s, but the integration over intermediate states must still be carried out. A more explicit representation of Eq. (2.32) is, for the surface case,

$$\hbar\omega_s(q)\varphi_s(q) - \frac{1}{2}\sum_{mnt}\int \frac{d^2k}{(2\pi)^2}\frac{V^s_{mn}(\mathbf{k},\mathbf{k}-\mathbf{q},\mathbf{q})V^t_{mn}(\mathbf{k},\mathbf{k}-\mathbf{q},\mathbf{q})}{\hbar[\omega_m(k)+\omega_n(|\mathbf{k}-\mathbf{q}|)-\omega(q)]}\varphi_t(q) = \hbar\omega(q)\varphi_s(q). \tag{3.2}$$

A. Excitations in two and three dimensions

Before we discuss the excitations of a layered liquid, let us briefly summarize the results of both the Feynman and the CBF-BW theories for the dispersion relation of the homogeneous two- and three-dimensional systems. The energetics of both systems has been reproduced in our ground-state theory quite satisfactorily.[1] Of course, the calculation of the excitation energies is an entirely different problem. In particular, it is well known that the simple Feynman theory, which leads in the bulk liquid to the famous Feynman dispersion relation $\omega(k) = \hbar k^2/2mS(k)$, predicts excitation energies which are, in the maxon-roton regime, about a factor of 2 too high. Thus, the starting point of an improved theory of excitations is much worse than the one of a variational theory for the ground state which neglects triplet correlations: Whereas triplet correlations contribute only a 10% correction to the ground-state energetics, the three-body vertex function appearing in Eq. (2.32) (and all possible higher corrections) must account for a factor of 2.

These considerations must be kept in mind when comparing the success of the ground-state theory with the success of the equivalent theory for excited states. Figure 2 is exemplary of the quality of different methods for calculating the spectrum. The Feynman dispersion curve is obtained from the calculated structure function $S(k)$ at experimental saturation density, and the CBF-corrected dispersion curve, at the same density, is the self-consistent solution of Eq. (2.32) for a homogeneous system. We also show the most complete solution of the equations of motion, to date,[14,15] which further improves upon the CBF calculation. The comparison with the experimental zero-sound dispersion allows us to assess the quantitative accuracy of each theory. The CBF calculation is identical to the one of Chang and Campbell,[9] but uses our more accurate input from the ground-state structure. From this figure, it is clear that the CBF theory contains the correct physics, i.e., most of the energetics of the roton minimum can be attributed to fluctuating short-range correlations. Figures 3 and 4 then show, over the stable regime of "bulk" densities, the calculated dispersion curves from (a) the Feynman theory in two and three dimension and (b) the CBF-corrected theory.

While for the bulk liquids it is possible[14,15] to carry out a nearly complete calculation of the dynamics determined by Eqs. (2.14) and (2.15); we have restricted our consideration to the simplest nontrivial level, Eq. (2.32), since the identical theory can also be implemented in the nonuniform system. In both the homogeneous two- and three-dimensional phase, better approximations for the three- and four-body densities can be (and have been) used in the equations of motion. The quantitative success of the method of time-dependent pair correlations in the calculation of the bulk phonon-roton spectrum of Refs. 14 and 15, which focuses more closely on the time dependence of the *short-range* structure than the uniform limit approximation used here, gives us confidence

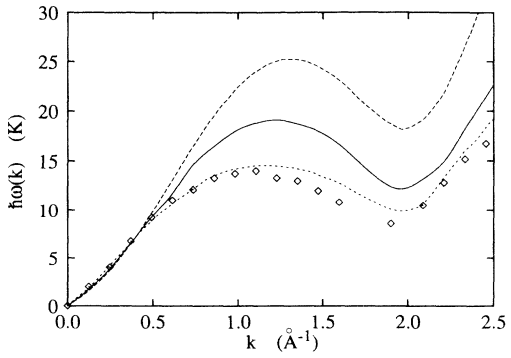

FIG. 2. The zero-sound dispersion relation is shown, for bulk *three-dimensional* ^{4}He, in (a) the Feynman approximation (long dashed line) and in (b) CBF-BW approximation (solid line, from Ref. 19), (c) from Ref. 15 (short-dashed line) at experimental saturation density $\rho = 0.021\,85$ Å^{-3} and (d) from experiments (Ref. 38) (diamonds).

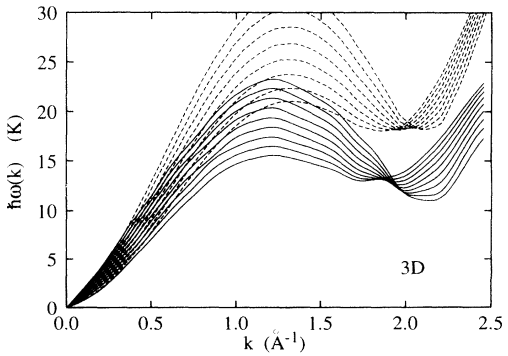

FIG. 3. The zero-sound dispersion relation is shown, for bulk *three-dimensional* ^{4}He, in (a) the Feynman approximation and in (b) CBF-BW approximation, for densities $\rho = 0.019,\ 0.020,\ldots,\ 0.026$ Å^{-3} (dashed lines) and in CBF-BW approximation (solid lines). The curves with the highest maxon peak and the lowest roton minimum always correspond to the highest density.

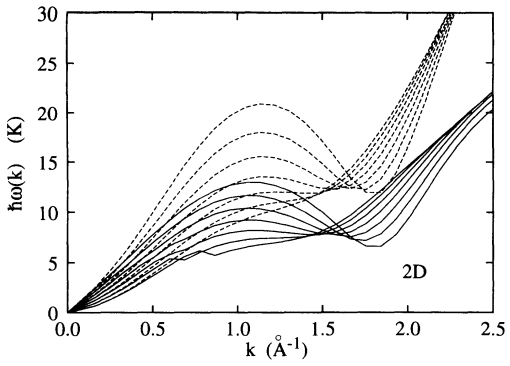

FIG. 4. The zero-sound dispersion relation is shown, for purely *two-dimensional* ^{4}He, in the Feynman approximation (dashed lines), and in CBF-BW approximation (solid lines), for coverages $n = 0.035, 0.040, \ldots, 0.065$ Å^{-2}. The curves with the highest maxon peak and the lowest roton minimum always correspond to the highest coverage. The slight "kinks" in the two curves corresponding to coverages $n = 0.035$ Å^{-2} and 0.040 Å^{-2} correspond to situations where, due to anomalous dispersion, multiple modes exist.

that the time dependence of the short-range structure is indeed the physical mechanism responsible for the roton minimum. It is now conceivable to use a similar scaling procedure as used in our ground-state calculations to improve the agreement with more complete evaluations of the same key quantities of the theory. In that case it was found that by scaling the elementary diagram contribution by a density and system independent constant factor we were able to obtain quantitative agreement with the entire equation of state for both the two- and three-dimensional liquids, but it had no noticeable effect on virtually any other quantity. We were confident then, that using the same scaling factor for the film geometry, was justified. The proper place to explore such improvements is in the homogeneous phases. Such exploration is important if a quantitatively precise theory of excitations, that is not only feasible but also physically *reliable*, is to be achieved in the case of quantum films. At the same time, the question as to how these corrections compare with time-dependent *triplet* correlations, which are ignored up to this point, should be studied.

B. Monolayer excitations energies

After these preparations, we are ready to study the low-lying excitations of liquid films. We first focus on monolayers since the physics of these systems is the most transparent. In our studies of the monolayer structure,[1] we were able to distinguish two characteristic types of behavior in these films: Films with *low* surface coverage can be approximated reasonably well by a two-dimensional system. However, when the coverage is increased, it will eventually be energetically favorable for the atoms to populate the third dimension rather than to further compress the atomic monolayer. A fair indication of when this crossover from "essentially" two to three dimensions occurs is when the incompressibility ($\equiv mc_3^2$) ceases to *increase* with increasing coverage. The population of states in the third dimension is accompanied by an abrupt drop of c_3, the third-sound velocity. The strength and range of the substrate potential $U_{\rm sub}(z)$ determine the coverage where this occurs. In the case under consideration here, the coverage $n_{\rm co}$ at the crossover is approximately $n_{\rm co} = 0.05$ Å^{-2}.

Figure 5 shows the dispersion curves for the lowest excitation energy solutions of the Feynman equation (2.20) and the CBF-BW equation (3.2) for a two-dimensional liquid and for atomic monolayers with coverages of $n = 0.035$, 0.045, 0.055, and 0.065 Å^{-2}. The monolayer calculations were carried out as follows: For a *real* target energy ω, the left-hand side of Eq. (3.2) is evaluated. To the extent that the mode sum in the CBF part had a pole, the momentum integral was treated as a principal value integral and the imaginary part was ignored. For such a fixed ω, the equation is then a Hermitean eigenvalue problem, which was solved for the lowest eigenstate and excitation energy. Using this energy as a new guess, the process was repeated until convergence was reached. The *lowest-energy* solution of the CBF-BW equation is real but this solution has, under certain circumstances, a negligible contribution to the dynamic structure function $S(q,\omega)$. We use the term "solution" here in a somewhat loose way, meaning the lowest *visible* solution. We will return to this question further below when we discuss anomalous dispersion and ripplon damping.

Our investigations of the ground-state structure in paper I show that the *lowest-coverage* film with $n = 0.035$ Å^{-2} is close to an instability against the formation of "two-dimensional droplets," whereas the *highest-coverage* film with $n = 0.065$ Å^{-2} is "almost" unstable against the formation of a second layer. Correspondingly, Fig. 5 shows a remarkable change in the spectrum of the lowest-lying excitation as a function of coverage: For low-coverage films, $n = 0.035$ and 0.045 Å^{-2}, the dispersion curve of the lowest mode is in close agreement with the one obtained for the two-dimensional model system. As the coverage is increased, the dispersion curve of the lowest mode starts to differ, already at relatively long wave numbers, significantly from the two-dimensional model. Moreover, we find a pronounced "kink" in both the Feynman approximation and the CBF result at momenta around $q_{\|} = 1.2$–1.3 Å^{-1} which we will identify momentarily as a level crossing. Also, the "roton minimum" is considerably less pronounced in the monolayer than in the two-dimensional model.

Our results can be interpreted on the basis of our ground-state calculations of paper I. In the lower stable coverage regime considered here, the excitations are essentially two-dimensional phonons. These are longitudinal phonons propagating in the thin film. For wave vectors shorter than 0.2 Å^{-1} these excitations are well described by the dispersion relation $\hbar\omega = \hbar c q_{\|}$. Near the low- and high-coverage instabilities the softening of this mode is clearly visible.

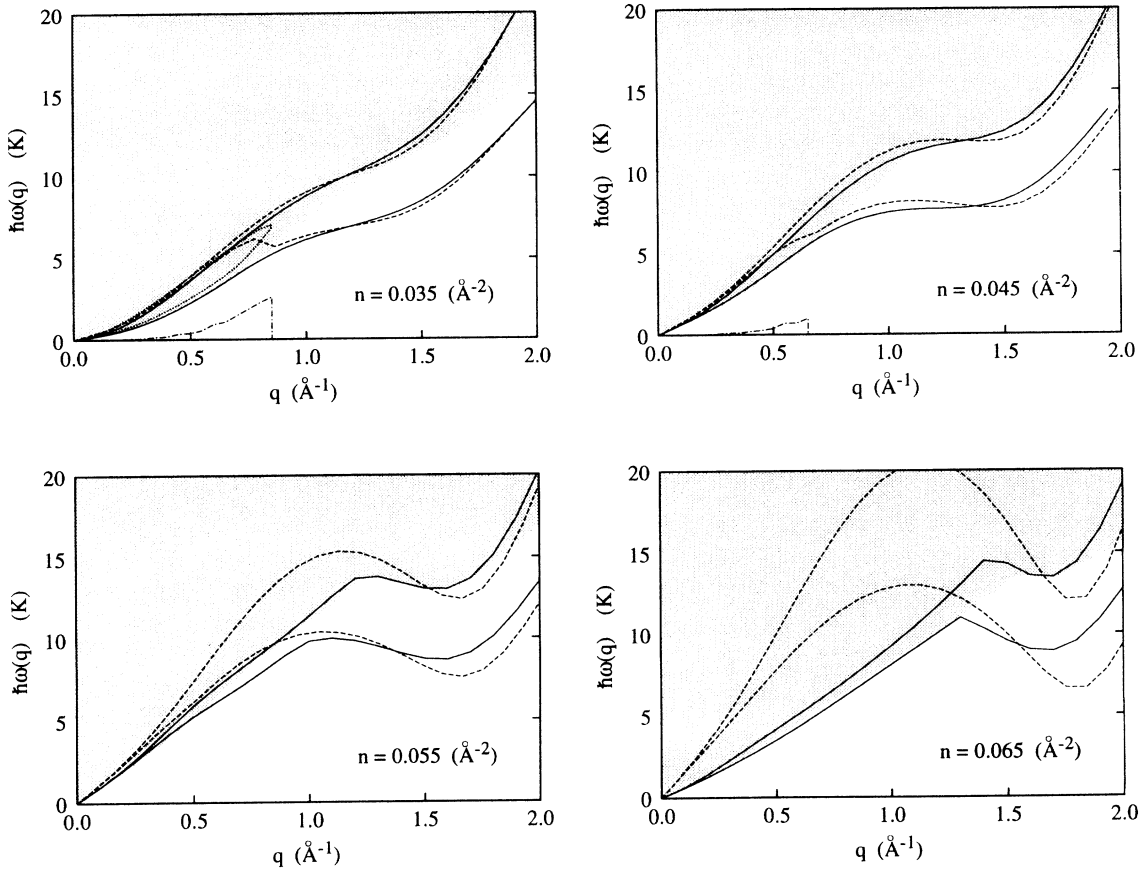

FIG. 5. Dispersion relation of the lowest excited state of monolayer films with coverages of $n = 0.035$, 0.045, 0.055, and 0.065 Å^{-2} (solid lines) and for two-dimensional ^{4}He at the same densities (dashed lines). The lower curves are the CBF-BW results, and the upper curves the results from the Feynman theory. The dash-dotted lines for $n = 0.035$ Å^{-2} and $n = 0.045$ Å^{-2} are the imaginary parts of modes lying slightly above $\omega_{\rm crit}(q)$. These modes are shown, in the case $n = 0.035$ Å^{-2}, as a closed dotted line. The gray-shaded area is the regime of energies $\omega > \omega_{\rm crit}(q)$ where the excitation energies become complex.

C. Monolayer transition densities

Above $n_{\rm co}$ the film becomes three dimensional. Accompanying this crossover is a new type of excitation, which corresponds to particle motion *out of* the symmetry plane. The effect is seen clearly in the *transition densities*, which are the time-dependent part of the total density. In the present geometry, these transition densities are of the form $\delta\rho_1(\mathbf{r};t) = \delta\rho_1(q_\parallel,z)e^{i(\mathbf{q}_\parallel\cdot\mathbf{r}_\parallel-\omega t)}$, and only the prefactor $\delta\rho_1(q_\parallel,z)$ is of physical interest. In our theory, the transition densities are given by the expansion in Eq. (2.31), which collapses to a single term (2.25) when the time-dependent pair correlations are omitted. Transition densities corresponding to the lowest-lying excitation are shown, for four monolayer films, in Fig. 6. At the two lower coverages, the transition densities are apparently essentially proportional to the ground-state density $\rho_1(\mathbf{r})$. The situation changes dramatically at the coverage of $n = 0.055$ Å^{-2}. At that coverage, we see, indeed, that the lowest mode qualifies for a surface excitation. However, this surface mode appears only at intermediate wave numbers, 0.5 Å$^{-1} \le q_\parallel \le 1.2$ Å^{-1}, whereas both the long-wavelength and the short-wavelength excitations have a strong overlap with the layer density.

The change of the character of the excitation is particularly pronounced at still shorter wavelengths; it appears at the place where the corresponding dispersion relation exhibits a sharp kink. Evidently, we encounter at this wavelength the familiar phenomenon of a level crossing. The same phenomenon has been observed in our earlier calculations[23,24] which were based on the Feynman approximation and partly[23] used a less accurate ground-state structure. The level crossing appears even sharper at the coverage, $n = 0.065$ Å^{-2}. At this coverage, the film is almost unstable against the elevation of particles into a second liquid layer. At this coverage the lowest mode is, up to the point of the level crossing around $q_\parallel \approx 1.3$ Å^{-1}, clearly a surface mode.

For coverages exceeding $n_{\rm co}$ more and more particles occupy positions elevated out of the two-dimensional plane and the incompressibility of the entire system shows a marked falloff. It is useful to comment on the relation between the long-wavelength transition densities and the incompressibility. The incompressibility referred

to here and in paper I refers to the entire film and is related to the speed of the lowest-lying mode. We now introduce a quantity which reflects the *local* compressibility corresponding to different regions (values of z) in the film. The concept of the local compressibility, which has been the subject of much studies in classical inhomogeneous fluids,[25] is most important near the layering transitions; obviously the divergence of the compressibility does not imply that the film is everywhere infinitely compressible.

We define the zero-temperature local compressibility, $\kappa(z)$, by

$$\frac{1}{mc^2} = \int dz\, \kappa(z)\,, \tag{3.3}$$

where we use c to denote the sound velocity. From the analysis of paper I, we immediately deduce

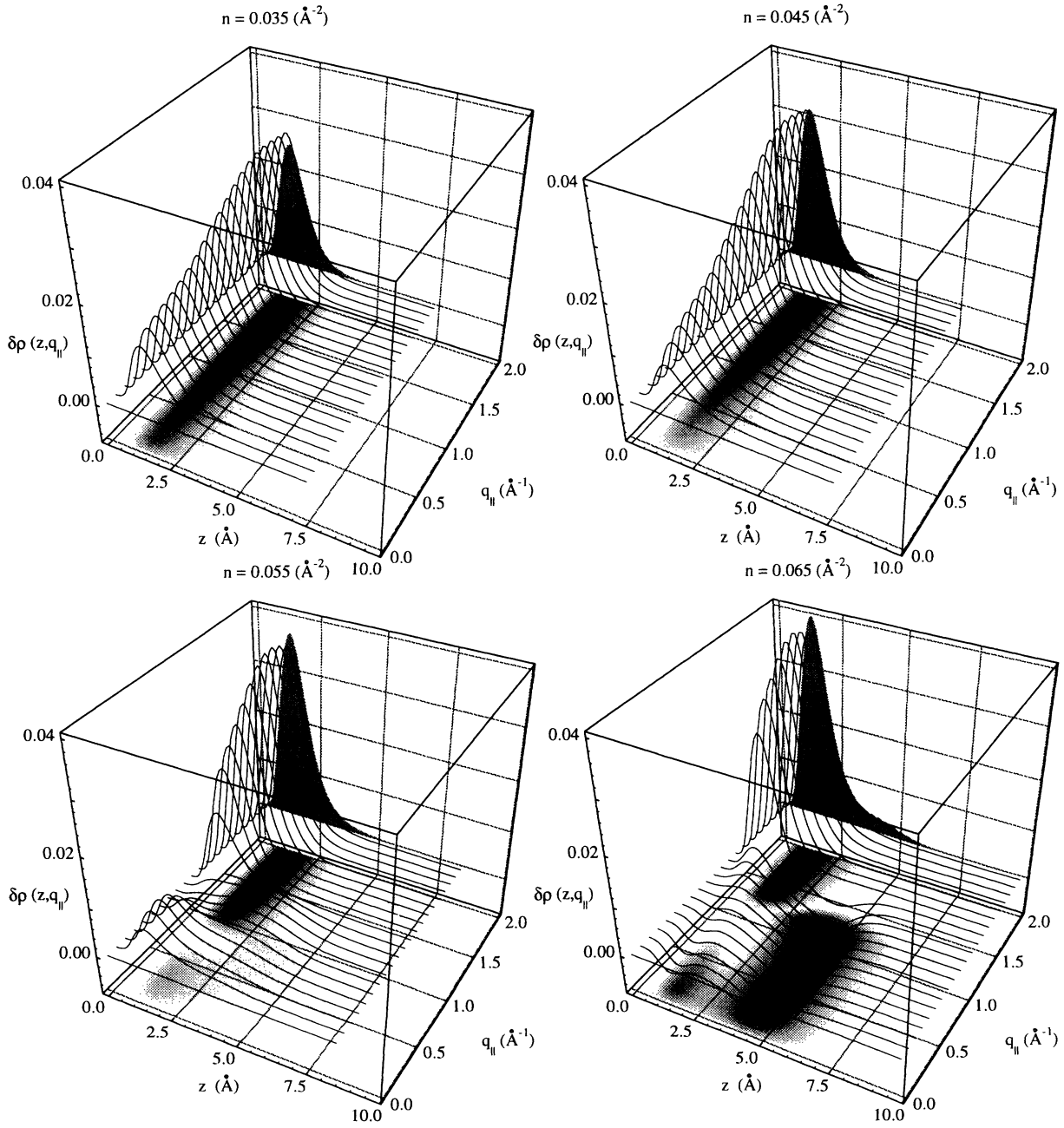

FIG. 6. Transition densities of the lowest excited state of monolayer films with coverages of $n = 0.035$ Å^{-2} (upper left), $n = 0.045$ Å^{-2} (upper right), $n = 0.055$ Å^{-2} (lower left) and $n = 0.065$ Å^{-2} (lower right). The shaded area in the background is the ground state profile, the grayscales at the bottom of the figure are a measure for the amplitude of $\delta\rho_1(z, q_{||})$.

$$\kappa(z) = \frac{2}{n}\int dz' \sqrt{\rho_1(z)}\left[H_1(q_\parallel = 0, z, z') + 2\hat{V}_{p\text{-}h}(q_\parallel = 0, z, z')\right]^{-1}\sqrt{\rho_1(z')} \ . \tag{3.4}$$

In the long-wavelength limit the transition densities (in both the Feynman and the CBF approximations) are given by Eq. (2.18), i.e.,

$$\delta\rho_1(\mathbf{r}) = \sqrt{\rho_1(\mathbf{r})}\frac{1}{\hbar\omega_n}H_1\psi_n(\mathbf{r}). \tag{3.5}$$

We now invert the convolution product of eigenvalue equation [Eq. (2.23) in paper I] for the ψ_n:

$$[H_1 + 2\tilde{V}_{p\text{-}h}] * H_1\psi_n = \hbar^2\omega_n^2\psi_n, \tag{3.6}$$

in the $q_\parallel = 0$ limit, and note that $\psi_o(z, q_\parallel \to 0) = \sqrt{\frac{2mc}{n\hbar q_\parallel}}\rho_1(\mathbf{r})$, where ψ_o denotes the lowest-energy eigenfunction. Comparing the results of these manipulations with Eq. (3.4) shows that, up to a prefactor containing a $q_\parallel$ and only z-independent quantities, the z dependence of the long-wavelength transition densities for the lowest energy mode can be directly interpreted as the local compressibility of the film.

In Fig. 7 the transition densities are shown for $q_\parallel = 0.1$ Å^{-1}. We also show the particle currents which will be the subject of the next section. In light of present discussion we can immediately identify the regions of high compressibility in the film. Most strikingly, at $n = 0.065$ Å^{-2}, we see that the outer shoulder that has formed in the density profile is highly compressible. Alternatively, atoms "residing" in this shoulder are very susceptible to low-energy, long-wavelength density fluctuations. On the contrary, at $n = 0.055$ Å^{-2}, the film is still very rigid at its outer surface at long wavelengths. This is the reason that a surface mode can only be excited at relatively high energies (and thus, large $q_\parallel$) at this coverage. As the film thickens the lowest energy needed to excite an out-of-plane mode steadily decreases. This is the mechanism that will eventually soften the surface mode so much that the dispersion law will change, from a linear dispersion relation, to a $q_\parallel^{3/2}$ law.

We conclude this subsection with a remark on the comparison between the CBF-BW and the Feynman theory of excitations. Clearly, the CBF theory provides a considerably improved agreement between the theoretical and experimental dispersion relations. Otherwise the qualitative features of the results (i.e., the appearance of a level crossing, and the manifestation of that in the transition densities) are in both theories essentially the same. This adds to our confidence that the much simpler Feynman theory is for many purposes sufficient to provide insight into the physical nature and mechanisms of excitations in nonuniform quantum liquids.

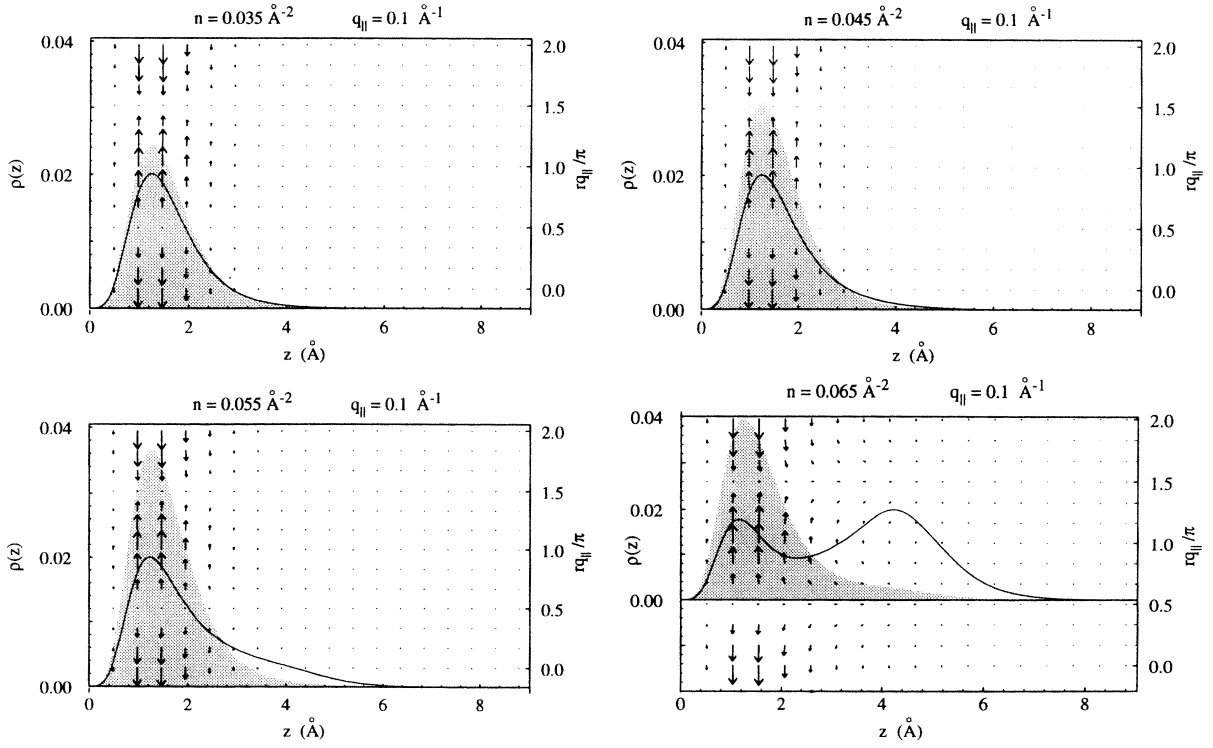

FIG. 7. The transition densities (solid lines) are shown for long-wavelength excitations $q_\parallel = 0.1$ Å^{-1} for four monolayer films with $n = 0.035$, 0.045, 0.055, and $n = 0.065$ Å^{-2}. The shaded area and the scale on the left side correspond to the background density. The vector fields superimposed to the figures show the particle currents corresponding to these excitations.

D. Particle currents

In the Feynman approximation, it is quite straightforward to calculate the particle currents from the excitation functions. Setting in Eq. (2.16) $\delta u_2(\mathbf{r},\mathbf{r}';t) = 0$ and recalling the connection (2.19) lets us express the current in terms of the Feynman excitation functions as

$$-i\hbar\mathbf{j}(\mathbf{r}) = \frac{\hbar^2}{2m}\rho_1(\mathbf{r})\nabla\left(\frac{\psi_n(\mathbf{r})}{\sqrt{\rho_1(\mathbf{r})}}\right). \tag{3.7}$$

In the specific, flat surface geometry, we can use the representation (3.1) of the excitation functions and obtain for the (real part of) current

$$-\hbar\mathbf{j}(\mathbf{r}) = \frac{\hbar^2}{2mL}\left[q_\parallel\cos(\mathbf{q}_\parallel\cdot\mathbf{r}_\parallel)\sqrt{\rho_1(\mathbf{r})}\psi_{n,\mathbf{q}_\parallel}(z)\ ,\ \rho_1(\mathbf{r})\sin(\mathbf{q}_\parallel\cdot\mathbf{r}_\parallel)\frac{d}{dz}\left(\frac{\psi_{n,\mathbf{q}_\parallel}(z)}{\sqrt{\rho_1(\mathbf{r})}}\right)\right]. \tag{3.8}$$

Equation (3.8) defines for each state a family of vector fields parametrized by the parallel momentum $\mathbf{q}_\parallel$.

Before we discuss the numerical results for our monolayer films, we should consider what is expected and where the limits of the Feynman approximations are. In the approximation (3.8), the current is derived from a velocity field

$$\mathbf{v}(\mathbf{r}) \equiv \frac{\mathbf{j}(\mathbf{r})}{\rho_1(\mathbf{r})} \sim \nabla\left(\frac{\psi_n(\mathbf{r})}{\sqrt{\rho_1(\mathbf{r})}}\right), \tag{3.9}$$

which is *curl free* because it corresponds to irrotational flow. Effects like the Feynman-Cohen backflow[20] are not expected to be described correctly, and will be considered in future work.

Turning now to the specific case of our liquid films, one would expect the following picture: As long as the excitation is predominantly a compression wave, the particle motion should be essentially in the direction of the wave propagation. However, in a surface mode, one would also expect particle motion *out of* the surface as well as in the direction of the wave propagation. More definite statements are difficult for adsorbed films, but an exact calculation is possible in the limit of an infinite half-space.

In that limit, the surface excitation is a ripplon and its excitation function can be calculated exactly[26] in the long-wavelength limit: The excitation function has the form

$$\psi_0(z,\mathbf{q}_\parallel) = C\sqrt{\rho_1(z)}e^{(q_\parallel z + i\mathbf{q}_\parallel\cdot\mathbf{r}_\parallel)} \tag{3.10}$$

and the Feynman current is

$$\mathbf{j}(\mathbf{r}) \sim \rho_1(z)\left[\cos(\mathbf{q}_\parallel\cdot\mathbf{r}_\parallel)\ ,\ \sin(\mathbf{q}_\parallel\cdot\mathbf{r}_\parallel)\right], \tag{3.11}$$

i.e., the current is *circular*.

The clearest transitions between the different characters of the excitation modes happen for the high-coverage monolayer $n = 0.065$ Å^{-2}, we therefore concentrate our discussion on this case. Figure 8 shows current patterns for three different wave numbers; one well within the "ripplon regime," $q_\parallel = 0.5$ Å^{-1}, and two, for $q_\parallel = 1.4$ Å^{-1}, $q_\parallel = 1.5$ Å^{-1} in the area of the roton minimum, above and below the wave number where the level crossing occurs. Further current patterns for very long-wavelength excitations are shown in Fig. 7. Note that the current patterns shown in these figures correspond to the Feynman

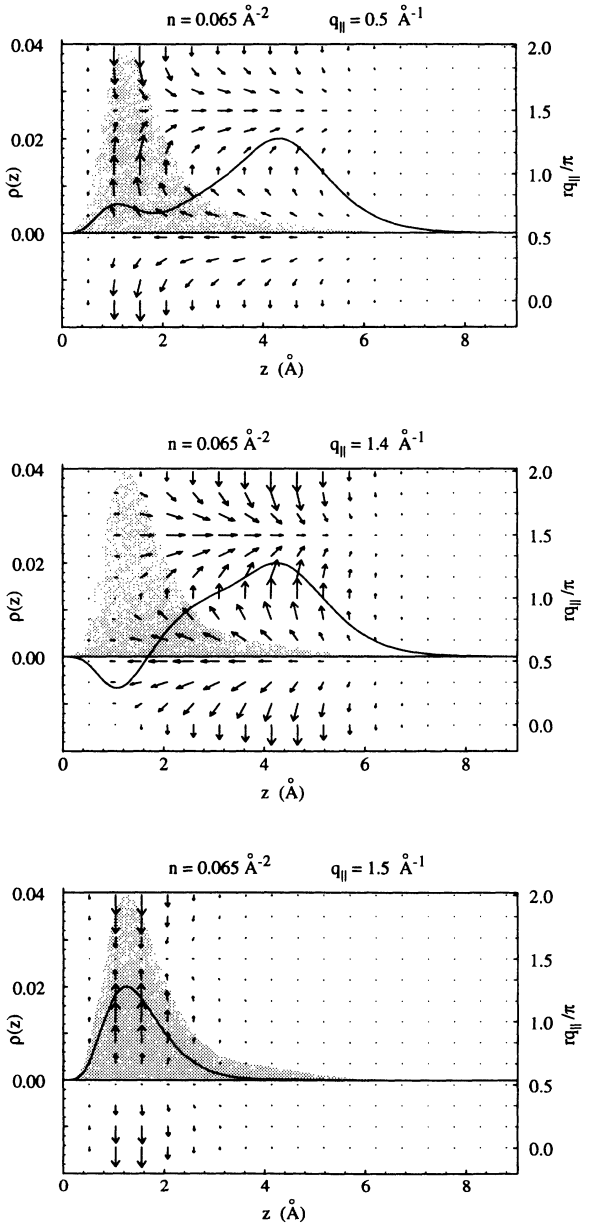

FIG. 8. Particle currents for the lowest excited state of a monolayer film with a coverage of $n = 0.065$ Å^{-2} and parallel momenta $q_\parallel = 0.5$ Å^{-1} (upper figure), $q_\parallel = 1.4$ Å^{-1} (middle figure) and , $q_\parallel = 1.5$ Å^{-1} (lower figure). The shaded area and the scale on the left side correspond to the background density, the solid line is the transition density.

dispersion curves (upper curves) in Fig. 5, in particular the wave number $q_{\|} = 1.4$ Å^{-1}, in Feynman approximation, is still a surface excitation whereas in the improved CBF-BW theory it is already a layer phonon.

The current patterns reflect more clearly than the transition densities the character of the different excitations. Before focusing on the details, note that the currents shown in these figures are drawn in a plane perpendicular to the substrate, and parallel to the direction of propagation of the wave. Parenthetically, one could also study the current in a plane *parallel* to the substrate. In particular in the roton regime, one should expect "backflow"-like patterns to appear in two-particle currents. However, the Feynman theory will not display such patterns and we therefore defer consideration of three-dimensional flow patterns to future studies.

We consider two cases: the $q_{\|}$ dependence of the currents, at constant coverage (n =0.065 Å^{-2}), and its coverage dependence at fixed $q_{\|}$. In the fixed coverage case, at *long* wavelengths ($q_{\|} = 0.1$ Å^{-1}) even though the mode appears to be a surface mode, most of the particle current is located within the first layer. At *intermediate* wavelengths ($q_{\|} = 0.5$ and 1.4 Å^{-1}), the current displays the circular flow pattern expected for a ripplon, whereas at *short* wavelengths ($q_{\|} = 1.5$ Å^{-1}), the current is again essentially a compression mode propagating in the first layer. This is consistent with the level-crossing picture. In the case of fixed $q_{\|}$ we will restrict ourselves to the long-wavelength limit and consider only the currents shown in Fig. 7. The most obvious point to be made is that the ripplon nature of the current, although weak for $n = 0.065$ Å^{-2} at $q_{\|} = 0.1$ Å^{-1}, is considerably enhanced relative to the one at $n = 0.055$ Å^{-2}. This observation complies well with the surface compressibility discussion in the last subsection.

From these studies of the transition densities and the particle currents we have to conclude that the mechanism of mode softening is quite different from the traditional ripplon picture. Conventionally, one would have expected that the ripplon and/or third-sound mode extends down to $q_{\|} = 0$, and that the strength of that mode increases as the film approaches the instability. This does not appear to be the case: Rather, momentum range of the surface excitation extends to longer and longer wavelengths.

E. Ripplon damping

The scenario of the development of the low-lying excitation energies can have interesting consequences on the damping of the ripplon and/or third sound mode. For the discussion, let us return to Eq. (2.32) and consider the right-hand side as a function of the energy ω, i.e., we define a function $\gamma_q(\omega)$ to be the lowest eigenvalue of the left hand side of the problem

$$\hbar\omega_s(q)\varphi_s(q) - \frac{1}{2}\sum_{mnt}\int \frac{d^2k}{(2\pi)^2}\frac{V^s_{mn}(\mathbf{k},\mathbf{k}-\mathbf{q},\mathbf{q})V^t_{mn}(\mathbf{k},\mathbf{k}-\mathbf{q},\mathbf{q})}{\hbar[\omega_m(k)+\omega_n(|\mathbf{k}-\mathbf{q}|)-\omega]}\varphi_t(q) = \hbar\gamma_q(\omega)\varphi_s(q), \tag{3.12}$$

where ω is now a free parameter, and $\varphi_s(\omega)$ the eigenvector corresponding to the eigenvalue $\gamma_q(\omega)$. Stability of the system requires that $\gamma_q(0) > 0$, and the structure of Eq. (3.12) has the consequence

$$\frac{d\gamma_q(\omega)}{d\omega} < 0 \tag{3.13}$$

when ω is small enough that the integrand has no pole. Therefore, it is guaranteed that a solution of the transcendental equation

$$\gamma_q(\omega) = \omega \tag{3.14}$$

exists which is *below* the lowest Feynman energy. For the discussion to follow, it is sufficient to concentrate on the lowest Feynman modes which we will denote with $\omega_0(q)$. Defining

$$\omega_{\rm crit}(q) = \min_k\left[\omega_0(k) + \omega_0(|\mathbf{k}-\mathbf{q}|)\right], \tag{3.15}$$

the condition for a *real* $\gamma_q(\omega)$ is, for fixed q,

$$\omega(q) < \omega_{\rm crit}(q). \tag{3.16}$$

If the Feynman spectrum is monotonic for $0 \le k \le q$, one has $\omega_{\rm crit}(q) = 2\omega_0(q/2)$, and if the spectrum is convex, this value will be *below* the lowest Feynman energy. This is the familiar consequence of anomalous dispersion. Clearly, the condition of anomalous dispersion is met whenever the lowest excitation becomes "soft."

Closer analysis of equation (3.12) (cf. Appendix) shows that the imaginary part of $\gamma_q(\omega)$ is discontinuous at $\omega \to \omega_{\rm crit}(q)$, and that the real part has a *logarithmic singularity* at that point. This singular behavior, together with Eq. (3.13) has the consequence that $\gamma_q(\omega) \to -\infty$ as $|\omega(q) - \omega_{\rm crit}(q)| \to 0$. Therefore, the *lowest* solution of the CBF-BW equation is always real, *albeit* it may be arbitrarily close to the singularity.

It is worth noting here that the analytic structure of the self-energy in two dimensions is quite different from the one in three dimensions[27] for the case of anomalous dispersion. In three dimensions, the imaginary part behaves as $\mathrm{Im}\gamma_q(\omega) \sim [\omega(q) - \omega_{\rm crit}(q)]$, and the real part as

$$\mathrm{Re}\gamma_q(\omega) \sim [\omega(q) - \omega_{\rm crit}(q)]\ln|\omega(q) - \omega_{\rm crit}(q)|.$$

Hence, the damping of any mode slightly above $\omega_{\rm crit}(q)$ is expected to be much smaller.

In our numerical applications of the full surface problem, we found that the logarithmic singularity around $\omega_{\rm crit}(q)$ is, for long wavelengths, quite narrow compared with the relevant energy scales in the problem [for example, $\omega_0(q)$]. For small q the solution of $\gamma_q(\omega) = \omega(q)$ is very close to $\omega_{\rm crit}(q)$, typical values of $\omega_{\rm crit}(q) - \omega_0(q)$ were 10^{-2} K or less. Hence $\gamma_q(\omega)$ has a very large slope.

However, the contribution of each mode to the dynamic structure function is proportional to the residue of the matrix

$$\left[\hbar(\omega_s(q)-\omega)\delta_{st} - \frac{1}{2}\sum_{mnt}\int \frac{d^2k}{(2\pi)^2}\frac{V^s_{mn}(\mathbf{k},\mathbf{k}-\mathbf{q},\mathbf{q})V^t_{mn}(\mathbf{k},\mathbf{k}-\mathbf{q},\mathbf{q})}{\hbar[\omega_m(k)+\omega_n(|\mathbf{k}-\mathbf{q}|)-\omega(q)]}\right]^{-1} \tag{3.17}$$

at the solution—it is therefore extremely small. For frequencies *above* the logarithmic singularity, the function $\gamma_q(\omega)$ is reasonably flat. Normally, one will find another solution in that frequency regime which will give a finite contribution to the residue. This solution will be the experimentally visible one. In this situation one cannot guarantee, *a priori*, that the solution is below the corresponding Feynman solution, although this was always found to be the case in our work. The analytic structure of the multiphonon correction term in a thin monolayer is very similar to the one of a two-dimensional liquid; more discussions of the above points will be given in the Appendix.

In Fig. 5 we see that the "visible" solution enters the regime $\omega > \omega_{\text{crit}}$ only at long wavelengths. When significant, we also show the imaginary part of the spectrum, calculated as described above. It appears that, as the *lower-coverage* instability is approached, the damping can be quite pronounced. Indeed, for the low-coverage case, our theory produces a linewidth on the order of 1 K. In contrast, neutron-scattering experiments done for ^{4}He on graphite,[28,29] at a temperature of 0.8 K, indicate that the characteristic linewidth, determined mainly by the experimental resolution, is on the order of 0.6–0.8 K. Consequently, a sufficiently low-temperature scattering experiment (so as to not destroy the structural phase transitions associated with the layered growth of the film) done over a range of coverages which include an instability, should be sensitive to this anomalous broadening. The main technical feat that must be overcome is to probe the very long-wavelength excitations; a situation which is yet to be realized in neutron-scattering experiments on the ^{4}He films.

As the coverage is increased, the lowest mode becomes "stiffer," the anomalous dispersion is reduced, and the damping is reduced. Interestingly enough, the same damping effect is not so pronounced at the high-end stability limit. At $n = 0.065$ Å^{-2}, the self-consistent solution of the CBF-BW equation is always below the "critical" energy ω_{crit}. Correspondingly, no imaginary part is shown in Fig. 5 for that coverage.

Our results suggest an interpretation of the "reentrant superfluidity" of ^{4}He films on graphite recently reported by Crowell and Reppy.[30] These authors report that on a graphite substrate superfluidity disappears before the completion of the second layer and reappears early in the third layer. The disappearance of the superfluidity before completion of the second layer can be thought of as being connected with the solidification of that layer. Indeed it is well known that the second layer, while initially liquid, freezes under the pressure of the growing third layer. Crowell and Reppy's second layer is, in our approach, modeled by a static substrate potential. Our first *liquid* layer should be identified with their third atomic layer on the substrate. The appearance of superfluidity would therefore be connected with the disappearance of damping of the lowest collective excitation. Another way to argue that superfluidity should disappear is that the Landau construction[31] is no longer possible when a mode becomes soft for long wavelengths.

Additional evidence for ripplon damping at very low coverage liquid monolayers is found in the data of Zimmerli, Mistura, and Chan[32] where no "third sound" is observed at low coverages. These experiments have been discussed, in light of the present theory, in Ref. 2.

An equally intriguing observation, made by Crowell and Reppy,[30] is that the amount of connected superfluid present, as determined by their torsional oscillator apparatus, is *not* simply proportional to the total amount ^{4}He present, but rather follows a sequence of rapid jumps and plateaus which they correlate to the completion of their third through seventh layers and at temperatures well below the Kosterlitz-Thouless transition temperatures. This is the very behavior, for the superfluid mass to total coverage, that the present theory predicts; underlying completed layers will continue to be superfluid (there is a substantial energy gap needed to create an excitation in them), while the outer most layer will contribute to the connected superfluid mass only when it is not in the coexistence regime, i.e., when the lowest mode is not soft. In the transition regions between two uniform configurations, the two-dimensional clusters on top of the "highest" uniform layer are disconnected from the superfluid and can couple, for example through hydrodynamic backflow, to the substrate. In that sense, these clusters behave very similar to single impurity atoms such as ^{3}He, whose effective mass can also be determined by torsional oscillator experiments.

The primary limitation for the applicability of our theory to experimental systems stems from assumptions made regarding the substrate interaction; in all cases the substrate has been assumed to be flat and rigid. For liquid helium on certain substrates such as graphite or solid hydrogen on glass, we believe that this assumption is valid for four reasons: (i) the phase separation for the *submonolayer* is found experimentally,[33] at almost exactly the coverage where one would expect it to occur on a perfectly flat substrate; (ii) corrugation effects should be reduced by the first two layers of solid helium for the graphite substrate; (iii) layering transitions have been seen experimentally in the growth of *solid* ^{4}He;[34] (iv) recent PIMC calculations[3] done on a corrugated surface have found evidence for layering transitions.

The width of the coexistence region will be influenced by several factors. It can be expected that the width should decrease with increasing temperature. Indeed, above the maximum critical temperature, for all layering transitions, it should be possible for the film to grow without cluster formation at any coverage. Furthermore, as the film thickness increases it is expected that sub-

sequent layering transitions should have lower and lower critical temperatures.

Another factor will influence the plateau width measured in a torsional oscillator: Growing clusters in the coexistence region can percolate before the film uniformly covers the underlying layer.[30] If this occurs, and the percolating cluster is superfluid, then superflow will occur even inside the coexistence region. Under these circumstances, torsional oscillator experiments will produce a plateau width that is reduced from that which is predicted by theory. The fact that percolation may very well be taking place is apparent from their experimental data. Percolation should affect the *high-coverage* side of the coexistence regions and inspection of their data always shows the expected "rounding" in that region.

We have also determined the ground-state structure for other substrate potentials. We find that layering transitions are quite insensitive to small variations in the well depth of graphite substrate potential,[1] however quantities such as the speed of sound are sensitive to this. For the slightly longer-range solid hydrogen on glass substrate, we again find multiple layering transitions.[1] In contrast to these, we find only one well-defined layering transition for a magnesium substrate. A second transition may occur but it is sufficiently weak that our numerical treatment is not necessarily accurate enough to make a definite statement. Most likely, it would be completely washed out at any finite temperature. Consequently, on a magnesium substrate, one would expect to see an abrupt onset of superfluidity around a coverage of $n = 0.04$ Å^{-2}, but no significant plateaus.

IV. DOUBLE- AND TRIPLE-LAYER EXCITATIONS

The monolayers discussed in the last section provide the simplest and cleanest picture of excitation energies and mechanisms. As the coverage is increased to two or more layers, excitations may extend over all liquid layers and also include the surface region. Figure 9 shows a typical set of dispersion relations. We have chosen, for the double layers, the three coverages $n = 0.105$ Å^{-2}, $n = 0.120$ Å^{-2}, and $n = 0.135$ Å^{-2}. The lowest coverage is close to an instability against the formation of two-dimensional clusters, the second one is a "most stable" case in the sense that the incompressibility has its maximum there, and the highest coverage is close to an instability against the elevation of particles into a third layer. Nevertheless, we see only very little dependence of the dispersion relation on the coverage. In particular in the low momentum "ripplon" regime up to about $q_{\|} = 1$ Å^{-1}, the dispersion relations are almost identical. The anomalous dispersion is very small and, consequently, we do not obtain any significant ripplon and/or third-sound damping; the imaginary part of the ripplon energy is never larger than 10^{-2} K. Significant differences are found only around the roton minimum, where the low-coverage modes are flatter. In particular there is no visible minimum for the lowest coverage of

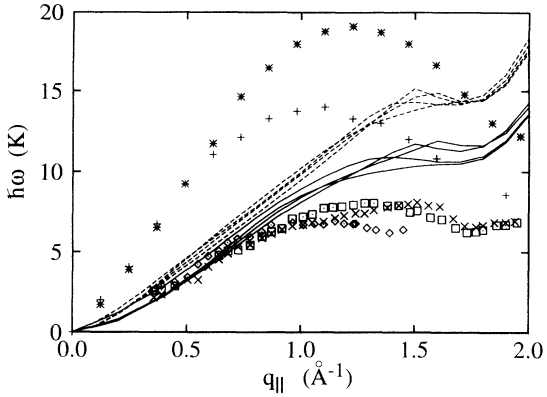

FIG. 9. The calculated dispersion relations for three double layer films with coverages $n = 0.105$ Å^{-2}, $n = 0.120$, and $n = 0.135$ Å^{-2} and a triple-layer film with $n = 0.170$ Å^{-2} in (a) CBF theory (solid lines) and (b) Feynman theory (dashed lines). The dispersion relations with the more pronounced roton minimum correspond to the higher coverages. Also shown are the data of Ref. 29 for a film with 1.54 (diamonds), 1.85 (squares), and 2.16 (crosses) liquid layers, the bulk phonon-roton spectrum (+ - symbols) and the calculated bulk phonon-roton spectrum in CBF theory (stars).

$n = 0.105$ Å^{-2}. The kink in the dispersion relation can again be attributed to a level crossing between the ripplon and a layer phonon, which has also been observed in the monolayers discussed in the preceding section, and our earlier work of Refs. 23 and 24. The same picture emerges at the level of the Feynman approximation. The size of the CBF correction and the accuracy of the prediction is comparable to the size of the same correction in the bulk, which we show along with the experimental phonon-roton spectrum.

The theoretically determined coverage dependence of the ripplon dispersion is qualitatively similar to the one found experimentally:[29] Similar to the theoretical dispersion curve, the experimental one is also weakly coverage dependent up to $q_{\|} = 1$ Å^{-1}. Above this wave vector, the 1.54-layer film shows a significant departure from the higher-coverage films. The 1.54-layer film, similar to our $n = 0.105$ Å^{-2} film, has a very shallow rotonlike minimum in its dispersion curve. It will become clear in the next section that the kinks observed in the higher-coverage experimental curves, near $q_{\|} = 1.5$ Å^{-1}, are also level crossings.

Somewhat more information on the nature of the excitations and confirmation of our interpretation of the level crossing can again be obtained from the transition densities and the particle currents. We show in Fig. 10 the transition densities corresponding to the four dispersion relations shown in Fig. 9, and in Fig. 11 the current patterns of a double-layer film close to an instability against promoting particles into a third layer. The case of a double layer is to some extent an "in-between" situation. Note that, as the population of the second layer is increased, the spectrum develops from a rather flat one (at $n = 0.105$ Å^{-2}) comparable with a low-density mono-

layer, to one that has a pronounced roton minimum at the high coverage, ($n = 0.135$ Å^{-2}). A similar picture is seen in the transition densities: At the *low populations* of the second layer, the lowest excitation propagates essentially in the second layer. At higher wave numbers we see again the typical picture of a level crossing. However, this level crossing is not between a "ripplonlike" and a "phononlike" mode, but rather between two phonons propagating in different layers. The situation changes as we increase the population of the second layer: The lowest mode develops into a surface mode and, at high wave numbers, *two* level crossings occur, one between a surface mode and a layer phonon, and the second one between two layer phonons. However, it takes a finite wave number for the usual circular current patterns of a surface mode to develop.

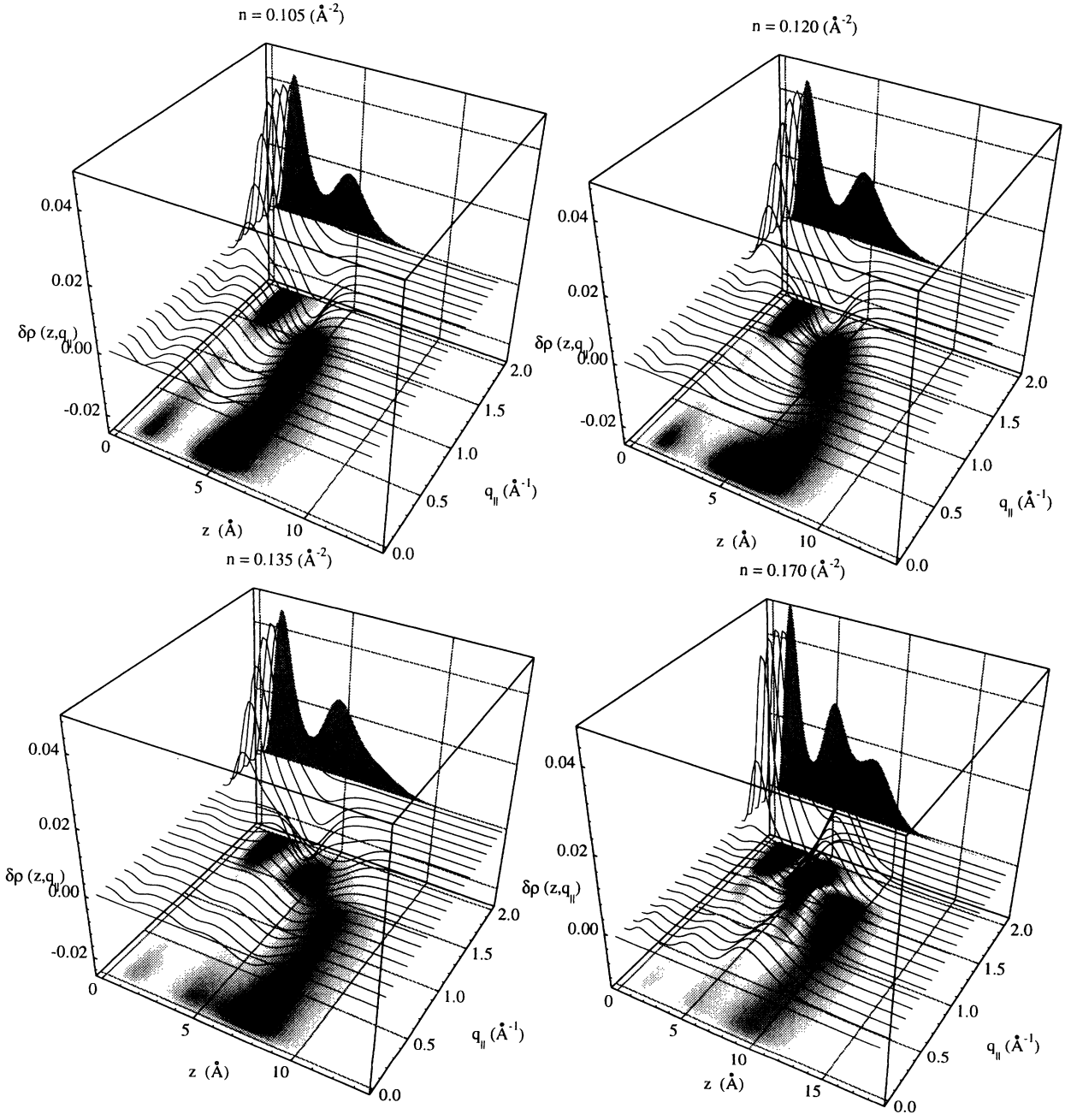

FIG. 10. Transition densities of the lowest excited state of a double layer films with coverages of $n = 0.105$ Å^{-2} (upper left), $n = 0.120$ Å^{-2} (upper right), $n = 0.135$ Å^{-2} (lower left), and a triple-layer films with $n = 0.170$ Å^{-2} (lower right). The shaded area in the background is the ground state profile, the grayscales at the bottom of the figure are a measure for the amplitude of $\delta\rho_1(z, q_{||})$.

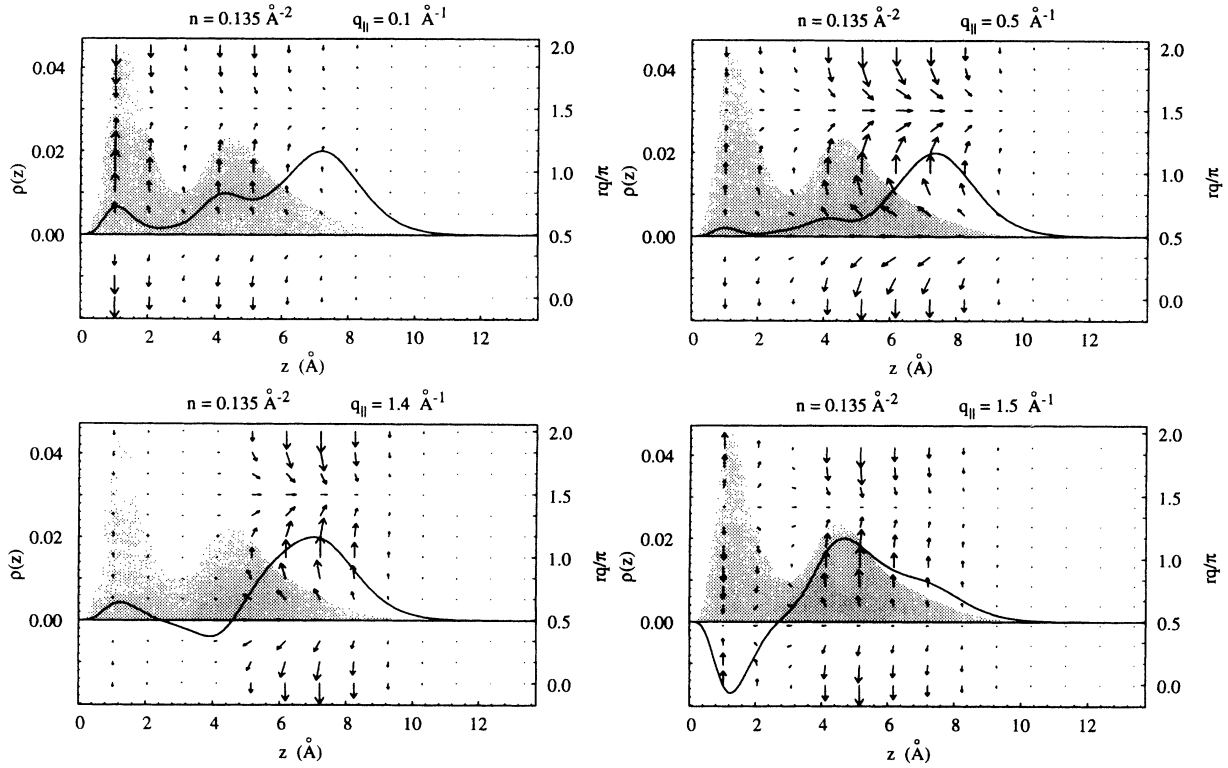

FIG. 11. Particle currents for the lowest excited state of a doublelayer film with a coverage of $n = 0.135$ Å^{-2}. See Fig. 8 for further explanations.

V. DYNAMIC STRUCTURE FUNCTION

A. Generalized Feynman theory of $S(q,\omega)$

The excitations of many-body systems such as quantum liquids, atoms, or nuclei are normally studied by scattering experiments. In these experiments, not only the lowest mode(s), but also a whole sequence of higher-lying modes can be excited, and their strength and dispersion gives further information on the structure of the system. The question of the location and the strength of the higher-lying modes is particularly relevant in the present case: The lowest-lying mode will, in the case of a finite system, *always* be the ripplon. However, as the system becomes bigger, the excitations will eventually be dominated by the bulk excitations, in other words the phonon-roton spectrum. These excitations have much higher energy than the ripplon, in fact they are, in the systems studied here, in the continuum [cf. Eq. (5.15) below]. The ripplon on the other hand should, while always present, lose relative strength and eventually become negligible.

When the probe is weak, the scattering cross section is given by the Born approximation by[35]

$$\frac{d^2\sigma}{d\Omega d\omega} = \frac{p_f}{p_i}\left(\frac{d\sigma}{d\Omega}\right)_0 S(\mathbf{q},\omega), \tag{5.1}$$

where $(d\sigma/d\Omega)_0$ is the differential scattering cross section for scattering from a single constituent, $\mathbf{p}_i$ and $\mathbf{p}_f$ are the initial and final momenta, $\mathbf{q} = \mathbf{p}_f - \mathbf{p}_i$ is the momentum transfer, and

$$S(\mathbf{q},\omega) = \sum_{n\neq 0} |\langle \Psi_n|\rho(\mathbf{q})|\Psi_0\rangle|^2 \delta(\hbar\omega - E_n + E_0) \tag{5.2}$$

is the dynamic structure function related to the response function by

$$S(\mathbf{q},\omega) = -\frac{1}{\pi}\mathrm{Im}\chi(\mathbf{q},\omega) \quad (\omega > 0). \tag{5.3}$$

The operator $\rho(\mathbf{q})$ introduced above is the *density operator*. Inelastic neutron scattering off helium films[28,29] can map out the dynamic structure function. Theoretically, the calculation of $S(\mathbf{q},\omega)$ requires knowledge of both the excitation spectrum $E_n - E_0$ and the complete set of *transition densities* $\langle \Psi_n|\rho(\mathbf{q})|\Psi_0\rangle$.

For practical calculations, a model of the excitation mechanisms such as the (generalized) Feynman theory described above is needed. Unfortunately, calculation of the dynamic structure function within the generalized theory that allows for time-dependent pair correlations is computationally quite time consuming. Since we have convinced ourselves by the studies of transition densities and particle currents that the simpler Feynman theory gives, for most applications, a qualitatively correct picture of the physics, we restrict our analysis of the dy-

namic structure function to the Feynman approximation $\delta u_2(\mathbf{r}_i,\mathbf{r}_j;t) = 0$. In this approximation, the present study is analogous to our earlier work;[23,24] it expands on that work by studying physically different cases and using a better structure of the static background.

The Feynman theory can be interpreted in terms of a linear-response theory with a *local* particle-hole interaction. The density-density response function is given in the random-phase approximation by the relation

$$\chi(\mathbf{r}_1,\mathbf{r}_2;\omega) = \chi_0(\mathbf{r}_1,\mathbf{r}_2;\omega) + \int d^3r_3 d^3r_4 \chi_0(\mathbf{r}_1,\mathbf{r}_3;\omega) \times V_{p\text{-}h}(\mathbf{r}_3,\mathbf{r}_4)\chi(\mathbf{r}_4,\mathbf{r}_2;\omega), \tag{5.4}$$

where $\chi_0(\mathbf{r}_1,\mathbf{r}_2;\omega)$ is the response function of a "noninteracting" system defined by the one-body Hamiltonian H_1:

$$\chi_0(\mathbf{r}_1,\mathbf{r}_2;\omega) = 2\sqrt{\rho_1(\mathbf{r}_1)}H_1\left[(\hbar\omega)^2 - H_1^2 + i\eta\right]^{-1} \times\sqrt{\rho_1(\mathbf{r}_2)}. \tag{5.5}$$

In Eq. (5.4), the local particle-hole interaction is the second variational derivative of the correlation energy functional with respect to the density:

$$V_{p\text{-}h}(\mathbf{r}_1,\mathbf{r}_2) \equiv \frac{\delta^2 E_c}{\delta\rho(\mathbf{r}_1)\delta\rho(\mathbf{r}_2)}. \tag{5.6}$$

The HNC theory employed in paper I provides a specific expression for this effective interaction.

Using the representation (5.5) of $\chi_0(\mathbf{r},\mathbf{r}';\omega)$, one can formally solve for the full response function $\chi(\mathbf{r},\mathbf{r}';\omega)$:

$$\chi(\mathbf{r},\mathbf{r}';\omega) = 2\sqrt{\rho_1(\mathbf{r})}\left\{\left[(\hbar\omega)^2 - H_1^2 - 2H_1\hat{V}_{p\text{-}h} + i\eta\right]^{-1} H_1\right\}\sqrt{\rho_1(\mathbf{r}')} = 2\sum_n \sqrt{\rho_1(\mathbf{r})}\phi_n(\mathbf{r})\frac{(\hbar\omega_n)^2}{(\hbar\omega)^2 - (\hbar\omega_n)^2 + i\eta}\phi_n(\mathbf{r}')\sqrt{\rho_1(\mathbf{r}')}, \tag{5.7}$$

where $\hat{V}_{p\text{-}h}(\mathbf{r},\mathbf{r}') \equiv \sqrt{\rho_1(\mathbf{r})}V_{p\text{-}h}(\mathbf{r},\mathbf{r}')\sqrt{\rho_1(\mathbf{r}')}$ and the $\phi_n(\mathbf{r})$ and the $\hbar\omega_n$ are the eigenfunctions and eigenvalues of the equation

$$\left[H_1^2 + 2H_1\hat{V}_{p\text{-}h}\right]\phi_n = (\hbar\omega_n)^2\phi_n. \tag{5.8}$$

In Eq. (5.8), we recover the Euler equation of the optimized HNC theory.[1]

From the density-density response function (5.7) one obtains finally the dynamic structure function

$$S(\mathbf{r},\mathbf{r}';\omega) = -\frac{1}{\pi}\mathrm{Im}\chi(\mathbf{r},\mathbf{r}';\omega) = \sqrt{\rho_1(\mathbf{r})}\phi_n(\mathbf{r})\phi_n(\mathbf{r}')\sqrt{\rho_1(\mathbf{r}')} \tag{5.9}$$

and static structure function (2.21)

$$S(\mathbf{r},\mathbf{r}') = -\frac{1}{\sqrt{\rho_1(\mathbf{r})\rho_1(\mathbf{r}')}}\int_{-\infty}^{\infty}\frac{d(\hbar\omega)}{2\pi}\mathrm{Im}\chi(\mathbf{r},\mathbf{r}',\omega) = \sum_n \phi_n(\mathbf{r})\phi_n(\mathbf{r}'). \tag{5.10}$$

In both equations (5.7) and (5.10), the summation over the frequencies is understood as an integration when the spectrum is continuous. The last step in the analysis is to identify the functions $\phi_n(\mathbf{r})$ of Eq. (5.8) with the excitation functions $\phi_n(\mathbf{r})$ introduced in Eq. (2.24). This final identification lets us write the dynamics structure function as

$$S(\mathbf{r},\mathbf{r}';\omega) = \delta\rho_\omega(\mathbf{r})\delta\rho_\omega(\mathbf{r}'). \tag{5.11}$$

Normally, the dynamic structure function is discussed in momentum space. In our geometry, the dynamic structure function is diagonal in the momentum $\mathbf{q}_\parallel$ parallel to the surface. Scattering experiments are performed at grazing angles to obtain a sufficient strength of the signal; we therefore consider only momenta parallel to the surface. Thus, we define the *diagonal* dynamic structure function in momentum space

$$S(q_\parallel;\omega) = \int dz\,dz'd^2r_\parallel e^{i\mathbf{q}_\parallel\cdot\mathbf{r}_\parallel}\sqrt{\rho_1(\mathbf{r})}S(\mathbf{r},\mathbf{r}';\omega)\sqrt{\rho_1(\mathbf{r}')} = |\delta\rho_\omega(q_\parallel)|^2 \tag{5.12}$$

with

$$\delta\rho_\omega(q_\parallel) = \int dz\,\delta\rho_\omega(z,q_\parallel) = \int dz\sqrt{\rho_1(z)}\phi_\omega(z,q_\parallel) = \left[\frac{\hbar q_\parallel^2}{2m\omega(q_\parallel)}\right]^{\frac{1}{2}}\int dz\sqrt{\rho_1(z)}\psi_\omega(z,q_\parallel). \tag{5.13}$$

The static structure function in the parallel direction, $S(q_\parallel)$, is then defined as

$$S(q_\parallel) = \frac{1}{n}\sum_\omega S(q_\parallel;\omega). \tag{5.14}$$

In order to analyze the character of the higher-lying resonances, it is again instructive to study the z dependence of $\delta\rho_\omega(z,q_\parallel)$. This can be done at the level of the Feynman approximation or within the generalized formalism which also contains fluctuating pair correlations $\delta u_2(\mathbf{r}_i,\mathbf{r}_j;t)$. For the lowest modes, we have discussed these transition densities above; our findings in the Feynman approximation are, for the lowest mode, qualita-

tively the same. For the higher-lying modes, transition densities have been discussed in Ref. 23; our results in the present case are similar and shall not be repeated here.

B. Monolayer dynamic structure

At the level of the Feynman approximation, our model for the dynamic structure function assumes nothing but the ability to compute the static structure function with good accuracy. The spectrum of excitation energies $\hbar\omega$ is discrete for energies smaller than the separation energy, i.e., for

$$\hbar\omega + \mu < \hbar^2 q_{\|}^2/2m, \tag{5.15}$$

otherwise it is continuous. When the eigenvalue equation (2.20) is discretized on a finite mesh, only a discrete subset of the continuum states is obtained. This set of states corresponds to excitation functions that vanish at the boundary of the discretization box. However, all functions appearing in the kernels of Eq. (2.20) vanish exponentially for large distances from the surface. One can therefore extend the mesh to large distances to obtain a very dense spectrum from which reliable information on the density of states can be extracted. We have typically discretized the eigenvalue problem (2.20) in a box of 50–100 Å as compared to our film thickness of about 10–15 Å. No matter how large the discretization box is, one will still obtain an approximation of $S(q,\omega)$ in the form of a series of δ functions,

$$S(q_{\|};\omega) \approx \sum_n |\delta\rho_\omega(q_{\|})|^2 \delta(\omega - \omega_n). \tag{5.16}$$

In order to smooth these δ functions, we have replaced them in Ref. 23 by a square-well function with the width of the energy spacing between two neighboring states. To obtain a somewhat smoother representation of the dynamic structure function and to allow for a comparison of the relative strength of both the discrete and the continuum states, we have decided in this work to replace the δ functions by Gaussians of width 0.5 K, i.e., we write

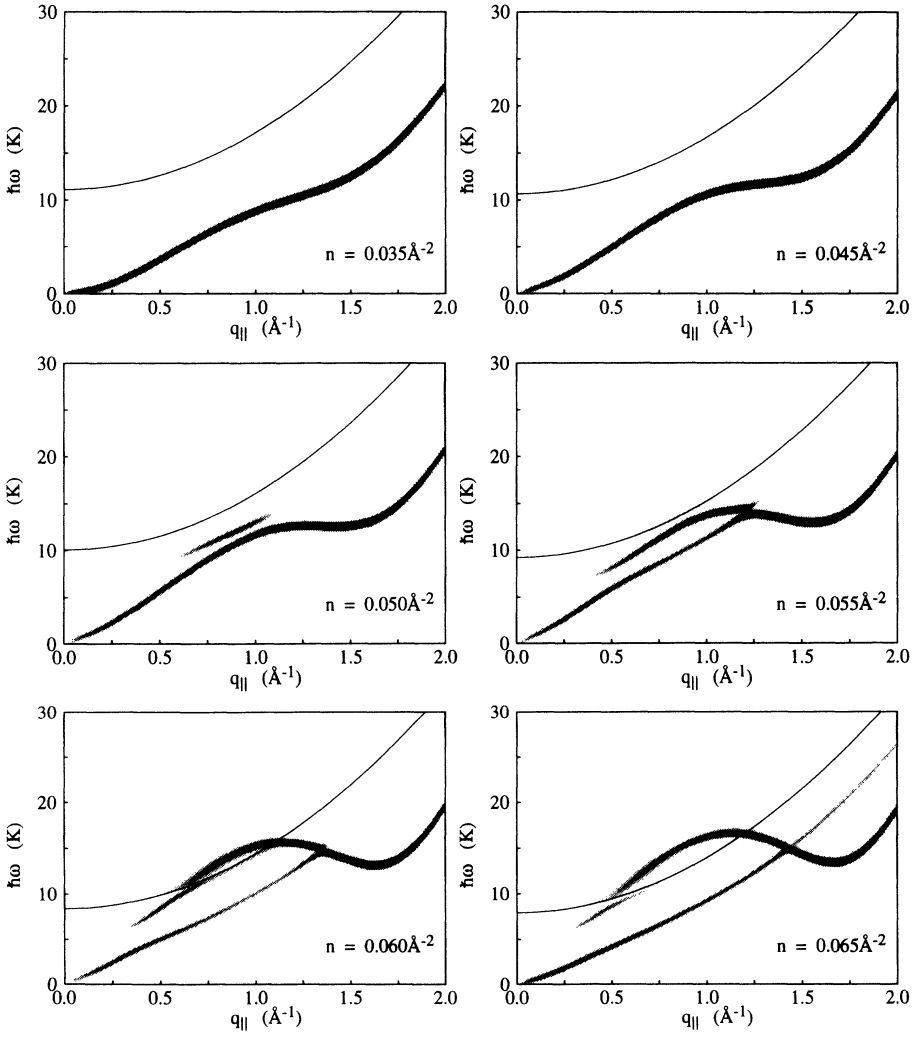

FIG. 12. The dynamic structure function $S(q_{\|},\omega)$ is shown, in the Feynman approximation, for a representative sample of monolayer films. The grayscale indicates the strength of $S(q_{\|},\omega)$, the parabolic line in the middle of the frames is the boundary of continuum states. All modes *below* this continuum are discrete in Feynman approximation; in order to display their relative strength we have artificially broadened these states by a Gaussian of approximately 0.5-K width.

$$S(q_{\|};\omega) \approx \sum_n |\delta\rho_\omega(q_{\|})|^2 \frac{1}{\epsilon\sqrt{\pi}} \exp\left[-\left(\frac{\omega-\omega_n}{\epsilon}\right)^2\right]. \tag{5.17}$$

A set of representative dynamic structure functions of liquid monolayers is shown in Fig. 12. In particular the relative strength of the higher-lying modes is seen more clearly than in Fig. 5, where we show only the dispersion relations. Note in particular that, starting with a coverage of $n = 0.055$ Å^{-2}, we see some strength appear in the continuum where a "mode" can no longer be defined unambiguously.

Figure 12 gives also a very clear account of the development of the monolayer excitations from a pure, longitudinal two-dimensional phonon, through a mixture between a phonon and a surface excitation, to the ripplon picture, including the level crossing at high momenta. At the very low coverage, we see essentially one mode, which we have identified above with a two-dimensional phonon. Also, the anomalous dispersion which leads to ripplon damping is clearly seen. As the coverage is increased, gradually a second mode, above the two-dimensional phonon but below the continuum, emerges but there appears to be very little interaction between these modes up to a coverage of $n = 0.055$ Å^{-2}. At that coverage we find the typical phonon-maxon-roton shape of the dispersion relation. At the same coverage we see, at intermediate wave numbers, an excitation that qualifies as a surface mode (cf. Fig. 6). Even though Fig. 6 shows results from the generalized theory, the transition densities in the corresponding Feynman approximation are very similar and have therefore not been shown. The case of $n = 0.055$ Å^{-2} is also interesting in the sense that the dispersion relation shows a small kink around $q_{\|} \approx 0.4$ Å^{-1}. With somewhat less confidence, one would be inclined to identify this kink with another level crossing. The nature of the mode is again confirmed by considering the transition density shown in Fig. 6; we see indeed that at this wave number the two-dimensional phonon turns into a surface excitation.

As the coverage is further increased, the appearance of two distinct types of excitations is clear: We see one type of excitation with the typical shape of the phonon-maxon-roton spectrum and one typical ripplon mode. The phonon-maxon-roton mode is for most wave numbers above the ripplon, and partly in the continuum. Around $q_{\|} \approx 1.4$ Å^{-1}, a clear level crossing occurs. The effect appears both in Feynman approximation and in the more general CBF-BW theory. A "hybridization" of the phonon and the ripplon, as recently proposed by Pitaevskii and Stringari[36] has, except at one singular momentum value, not been observed.

C. Multilayer dynamic structure

Figure 13 shows finally the dynamic structure function, in the Feynman approximation, for the four examples of double- and triple-layer films discussed above. In essence, we see the same picture as in the monolayers: a strong low-lying mode with the typical shape of a ripplon dispersion relation, and a high-lying mode with the shape of a phonon-maxon-roton spectrum. Unlike in the monolayer case, we find several other dispersion branches. To the extent that these modes can be clearly identified, they correspond mostly to phonons propagating in individual layers. Of course, the higher the energy of the mode,

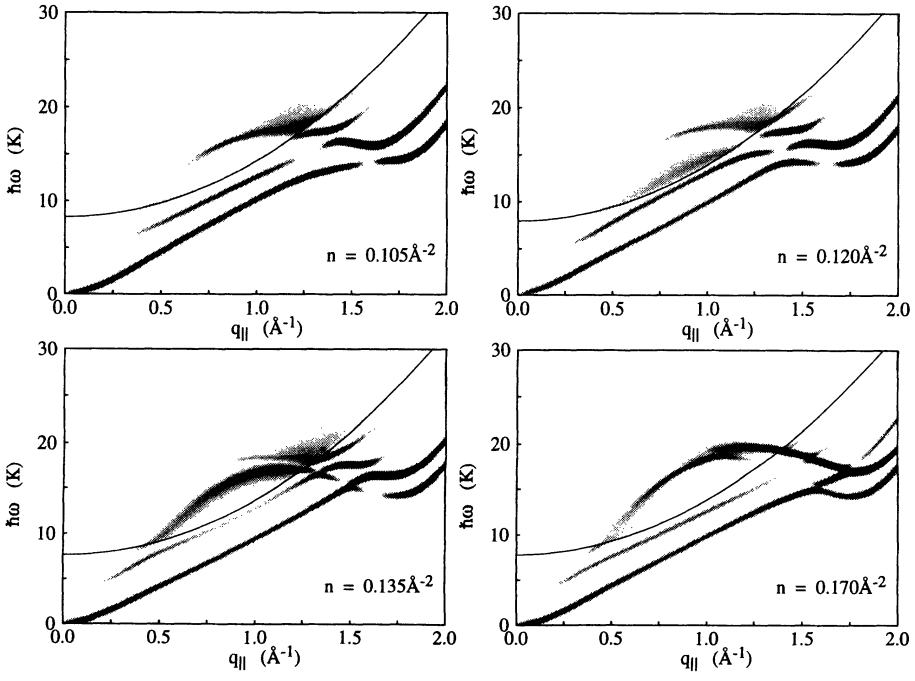

FIG. 13. Same as Fig. 12 for double- and triple-layer films for four different coverages.

the more nodes it will have and a clear identification becomes increasingly difficult. Our findings for multilayer excitations are in essential agreement with our earlier work;[23] the improved description of the background has some effect on the curvature of the dispersion relations in the vicinity of the roton minimum, but causes very few changes of the overall picture. This gives strong support for our assessment that the simple hypernetted chain approximation for the ground-state structure contains the essential physics of the system; extensions of the theory provide quantitative improvements, but little qualitative change. This is also true for the Feynman approximation of the excited states.

The question can now be asked how well does our theoretical picture of the excitations compare to experimental results. In Fig. 14, the experimental dynamic structure function for a triple-layer film is shown. The experiment[29] was performed at the time-of-flight spectrometer IN6 at the Insitute Laue-Langevin's reactor. The scattering sample consisted of ^{4}He adsorbed to graphite (Paypex), and was kept at a temperature of 0.65 K. The scattering is done at grazing angles. Each experimental curve within the family of curves, corresponds to a different wave vector q. The wave vectors range between 0.25 and 2.0 Å^{-1} and occur at approximately equal intervals. For bulk helium, the largest wave vector corresponds to the position of the roton minimum. We have vertically displaced $S(q,\omega)$ for each q to provide a clear representation of the excitations. In the figure, symbols have been added to indicate the positions of the various excitations. It is clear from the figure that, already for three layers, there is a rather strong signal coming from the mode that will evolve into the bulk phonon-maxon-roton spectrum. This may indicate that capillary condensation is occurring between the graphite crystallites. The low-energy surface excitation is equally clear from this figure and has been shown, for other coverages, in Fig. 9. At this coverage, it is appropriate to refer to this mode as being a ripplon.

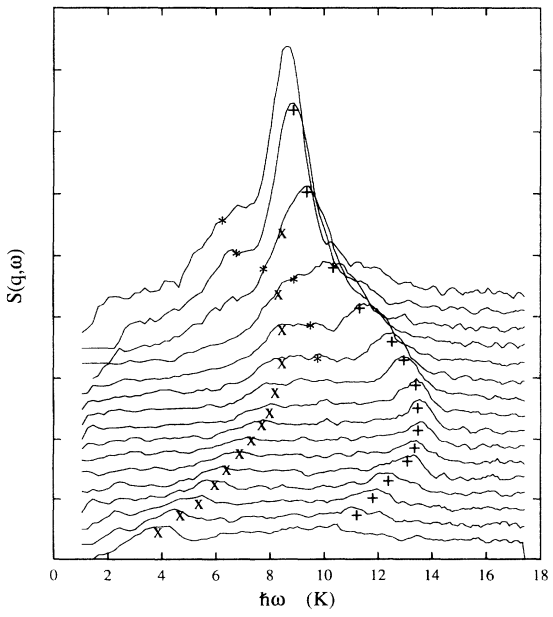

FIG. 14. The experimental $S(q,\omega)$ for a triple-layer film. The experimental data (solid curves), the phonon-maxon-roton mode (+), the ripplon (×), and a layer-phonon mode (*), are shown. Each experimental curve corresponds to a different wave vector (See text for discussion).

Another intriguing aspect is the observation that, between the phonon-roton excitation and the ripplon, there is a plateau in the strength of $S(q,\omega)$. Indeed, there is too much scattering to be explained by the phonon-roton mode (whose experimentally determined maximum linewidth is obvious from the figure), the surface mode, and multiphonon contributions. The latter can be quite safely ruled out, as a possible cause for the large plateau, by looking above the phonon-roton mode. There it is seen that multiphonon excitations produce very little scattering at this low temperature. An explanation for the extra scattering is provided by the theory; these are layer-phonon modes that occur between these two excitations and begin to be significant in $S(q,\omega)$ at wave vectors above 1.0 Å^{-1}. In fact, the possibility of seeing at least one of these modes is very evident from Fig. 14. A rather clear mode has been indicated by a line of *'s in that figure. It is very interesting that that mode actually appears to level cross with the surface mode, and for q near the roton minimum, where it has emerged out of the continuum, the full strength of the mode is shown. It is also very convincing that the sharp kink seen in the surface mode, in this figure and for those in Fig. 9, are very similar to the sharp kinks observed in the theoretical values where level crossings occur. It is equally important to note that the strength of the surface mode, in the experimental $S(q,\omega)$ actually continues for q above the level crossing. This is not obvious from the figure but follows by an analysis of the data which involves studying the linewidth of the surface excitation through the level-crossing region; below and above the level crossing there is a clearly defined *shoulder* in $S(q,\omega)$ which is the surface mode. This is again consistent with the theoretical calculations. While these experimental observations should be regarded as preliminary, they are extremely promising and have prompted new investigations using neutron scattering.

VI. SUMMARY AND OUTLOOK

We have discussed in this paper the excitation spectrum of adsorbed films of ^{4}He within a generalized Feynman theory of excited states. Formally, this is the first application of the theory to nonuniform systems. In this work, we have adopted the strategy of Saarela and coworkers[13–15] and developed the theory from the starting point of time-dependent pair correlations. The approach has the appealing feature that it attributes much of the excitation mechanism in the vicinity of the roton minimum to fluctuating short-range correlations. We hasten to point out that the same working formulas can also be derived by correlated-basis functions theory.[18] This is, theoretically, a very satisfactory situation since the derivation of the basic equations of the theory is a mat-

ter of strategy, and not of substance.

We have seen in our comparisons that the simpler Feynman theory applied here provides, for most effects, a physically plausible and appealing qualitative picture of the excitation spectrum of adsorbed films. A number of effects are, however, new. Most important is our result from paper I that the growth of the film does not happen continuously, but in a number of discrete steps corresponding to the formation of mono-, double-, and triple layers. Along with the structural phase transitions connected with this discontinuous growth are "mode softenings" which lead to anomalous dispersion and possibly ripplon damping. We found in our calculations that the effect of ripplon damping is noticeable only for monolayer films. This finding is consistent with the observation of Zimmerli, Mistura, and Chan[32] that no "third sound" is observed at low coverages, and those of Crowell and Reppy[30] on "reentrant superfluidity" in the third layer.

ACKNOWLEDGMENTS

The work was supported, in part, by the North Atlantic Treaty Organization under a Grant awarded in 1992 (to B.E.C), and the National Science Foundation under Grants No. PHY91-08066 and INT90-14040 (to E. K.) and PHY89-04035 to the Institute for Theoretical Physics (ITP) in Santa Barbara, and by the Academy of Finland (to M.S.). E.K. thanks the Institute Laue Langevin, where this work was started, and the ITP, where it was completed, for hospitality. Discussions with G. Agnolet, C. E. Campbell, P. Crowell, H. Godfrin, P. Leiderer, P. Nozières, and W. M. Saslow are gratefully acknowledged. Special thanks are given to H. Godfrin, V. Frank, and P. Leiderer for use of their unpublished data used in Fig. 14.

APPENDIX: ANALYTIC STRUCTURE OF THE CBF-BW SELF-ENERGY

In this appendix, we study the analytic structure of the CBF-BW self-energy as a function of an external frequency ω. We restrict the investigation to the simpler case of the two-dimensional system, which is identical to Eq. (2.32) when the summation over the discrete quantum numbers is restricted to the lowest state. In that limit, the Brillouin-Wigner eigenvalue problem reduces to a scalar equation, and the CBF self-energy $\gamma_q(\omega)$ is of the form

$$\gamma_q(\omega) = \hbar\omega_0(q) - \frac{1}{2}\int \frac{d^2k}{(2\pi)^2} \frac{|V(k,|\mathbf{k}-\mathbf{q}|,q)|^2}{\hbar[\omega_0(k)+\omega_0(|\mathbf{k}-\mathbf{q}|)-\omega(q)+i\eta]}. \tag{A1}$$

We are specifically interested in values of the energy where the function $\gamma_q(\omega)$ becomes complex. We assume that the lowest mode (or the Feynman phonon in two dimensions) $\omega_0(k)$ is a monotonic function of k. This restricts our analysis to the low-momentum regime which is acceptable since this is the only regime where we found complex modes below the Feynman spectrum. Defining [cf. Eq. (3.15)]

$$\omega_{\rm crit}(q) = \min_k [\omega_0(k) + \omega_0(|\mathbf{k}-\mathbf{q}|)], \tag{A2}$$

the condition for a *real* $\gamma_q(\omega)$ is, for fixed q,

$$\omega(q) < \omega_{\rm crit}(q). \tag{A3}$$

If the Feynman spectrum is monotonic for $0 \le k \le q$, the minimum value of $\omega_0(|\mathbf{k}-\mathbf{q}|)$ will be assumed when $\mathbf{k}$ and $\mathbf{q}$ are antiparallel, i.e., $\omega_0(|\mathbf{k}-\mathbf{q}|) = \omega_0(|k-q|)$. Due to symmetry, the function $\omega_0(k)+\omega_0(|k-q|)$ has an extremum for $k = q/2$, i.e., one has

$$\omega_{\rm crit}(q) = 2\omega_0(q/2). \tag{A4}$$

If the spectrum is convex, this extremum is a minimum, and its value is *below* the lowest Feynman energy for the same momentum q.

To evaluate the imaginary part of the integral (A1) for $\omega \approx \omega_{\rm crit}$ it is sufficient to consider the area where the angle θ between $\mathbf{k}$ and $\mathbf{q}$ is close to zero, i.e.,

$$\mathrm{Im}\gamma_q(\omega) \approx -\frac{1}{2}\mathrm{Im}\int \frac{d^2k}{(2\pi)^2} \frac{|V(k,|k-q|,q)|^2}{\hbar[\omega_0(k)+\omega_0(|\mathbf{k}-\mathbf{q}|)-\omega+i\eta]}. \tag{A5}$$

Next we expand the energy denominator in the vicinity of it's minimum value, $\omega_{\rm crit}(q)$. Letting $p = |\mathbf{k}-\mathbf{q}|$, we have

$$\begin{aligned}\omega_0(k)+\omega_0(p) &= 2\omega_0(q/2) + \omega'(p+k-q) \\ &\quad + \frac{1}{2}\omega''\left[(k-q/2)^2 + (p-q/2)^2\right] \\ &= 2\omega_0(q/2) + \frac{q}{2}\omega''\Bigg[\lambda(p+k-q) \\ &\quad + \frac{1}{q}\left(k^2+p^2-q^2/2\right)\Bigg],\end{aligned} \tag{A6}$$

where

$$\omega' = \left.\frac{d\omega_0(q)}{dq}\right|_{q/2}, \quad \omega'' = \left.\frac{d^2\omega_0(q)}{dq^2}\right|_{q/2} \tag{A7}$$

and

$$\lambda = \frac{2\omega'}{k\omega''} - 1. \tag{A8}$$

For $\cos\theta \approx 1$, we can also expand (recall that we are considering momentum transfers $k \approx q/2$):

$$\begin{aligned}p &= \sqrt{k^2+q^2-2kq+2kq(1-\cos\theta)} \\ &\approx q-k+\frac{kq}{(q-k)}(1-\cos\theta) \\ &\approx q-k+(4k-q)(1-\cos\theta)\end{aligned} \tag{A9}$$

and therefore

$$\omega(k)+\omega(p)=2\omega(q/2)+\frac{q^2\omega''}{2}\left[\lambda\left(4\frac{k}{q}-1\right)(1-\cos\theta)+\frac{2k}{q}\left(\frac{k}{q}-\cos\theta\right)+\frac{1}{2}\right]. \quad \text{(A10)}$$

This form of the energy denominator is correct, to second order in the momentum, in the vicinity of it's minimum value and for small angles. We can now carry out the angle integration and find

$$\mathrm{Im}\gamma_q(\omega)\approx-\frac{1}{2}\mathrm{Im}\int_0^\infty\frac{k\,dk}{(2\pi)^2}\int_0^{2\pi}d\theta\frac{|V(k,|k-q|,q)|^2}{A+B\cos\theta}$$

$$=-\frac{1}{4\pi}\mathrm{Im}\int_0^\infty k\,dk\frac{|V(k,|k-q|,q)|^2}{\hbar\sqrt{A^2-B^2}} \quad \text{(A11)}$$

with

$$A=2\omega_0(q/2)+\frac{q^2\omega''}{2}\left[\lambda\left(4\frac{k}{q}-1\right)+\frac{2k^2}{q^2}+\frac{1}{2}\right]-\omega+i\eta \quad \text{(A12)}$$

and

$$B=-\frac{q^2\omega''}{2}\left[\lambda\left(4\frac{k}{q}-1\right)+\frac{2k}{q}\right]. \quad \text{(A13)}$$

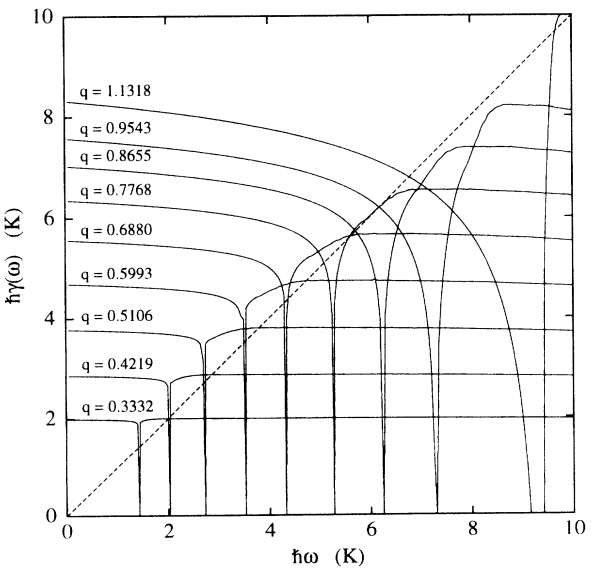

FIG. 15. The CBF self-energy $\gamma_q(\omega)$ is shown, for two-dimensional ^{4}He, as a function of ω for a sequence of momentum values for $n=0.035$ Å^{-2}. Solutions of the CBF-BW equations correspond to the points $\gamma_q(\omega)=\omega$ along the dotted line. Clearly, for $q<0.77$ Å^{-1} one has three solutions. It is also clearly seen that the logarithmic singularity is extremely narrow at small momenta.

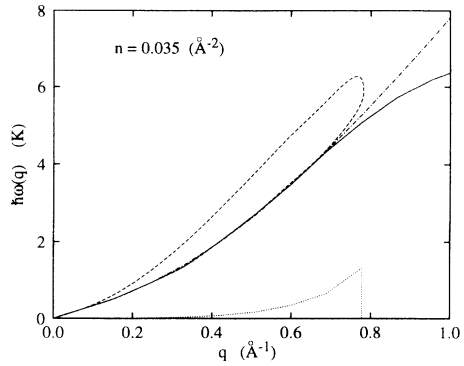

FIG. 16. The three long-wavelength "solutions" of the CBF-BW equation in two-dimensional ^{4}He for $n=0.035$ Å^{-2}. The solid line is the lowest solution of the CBF-BW equation, the dashed loop the two solutions above $\hbar\omega_{\mathrm{crit}}(q)$ (dash-dotted line) and the dotted line at the bottom of the figure is the imaginary part of the highest solution.

For $k\approx q/2$ and $\omega\approx 2\omega_0(q/2)$, we can further simplify

$$A^2-B^2=2k\omega'\omega''(k-k_-)(k-k_+) \quad \text{(A14)}$$

with

$$k_\pm=\frac{q}{2}\pm\sqrt{\frac{\omega-2\omega_0(k/2)}{q^2\omega''}}. \quad \text{(A15)}$$

For $\omega>2\omega_0(k/2)$ and $k_-<k<k_+$, the integrand is imaginary, and we get

$$\mathrm{Im}\gamma_q(\omega)\approx\frac{\left|V\left(\frac{q}{2},\frac{q}{2},q\right)\right|^2}{4\pi}\times\int_{k_-}^{k_+}\frac{k\,dk}{\hbar\sqrt{2k\omega'\omega''(k-k_-)(k_+-k)}}=q\frac{\left|V\left(\frac{q}{2},\frac{q}{2},q\right)\right|^2}{4\hbar\sqrt{2q\omega'\omega''}}, \quad \text{(A16)}$$

whereas the imaginary part is zero for $\omega<\omega_{\mathrm{crit}}$. With this, we have demonstrated that the imaginary part of the CBF self-energy has a finite discontinuity at $\omega=\omega_{\mathrm{crit}}$. Analyticity arguments[37] are then sufficient to show that the real part must have a logarithmic singularity at the same place, and to determine the strength of that logarithmic singularity.

Figure 15 shows the CBF-BW self-energy, for a low density two-dimensional case, as a function of momentum q and energy $\hbar\omega$. The logarithmic singularity at $\omega=\omega_{\mathrm{crit}}(q)$ is clearly seen, also that this singularity is, for low momenta, very sharp and permits under certain circumstances three solutions. These three solutions are shown in Fig. 16. There, the dash-dotted line is the boundary $\hbar\omega_{\mathrm{crit}}(k)$ above which all solutions are complex, and the dashed loop is the solution of the *real part* of the CBF-BW equation. Also clearly seen is the *imaginary* part if the complex solution peaks just before the "mode" disappears.

[1] B. E. Clements, J. L. Epstein, E. Krotscheck, and M. Saarela, Phys. Rev. B **48**, 7450 (1993).
[2] B. E. Clements, E. Krotscheck, and H. J. Lauter, Phys. Rev. Lett. **70**, 1287 (1993).
[3] M. Wagner and D. Ceperley, J. Low Temp. Phys. **94**, 185 (1994).
[4] C. C. Chang and M. Cohen, Phys. Rev. B **11**, 1059 (1975).
[5] D. O. Edwards and W. F. Saam, in *Progress in Low Temperature Physics*, edited by D. F. Brewer (North-Holland, New York, 1978), Vol. 7A, p. 282.
[6] R. A. Aziz *et al.*, J. Chem. Phys. **70**, 4330 (1979).
[7] E. Feenberg, *Theory of Quantum Liquids* (Academic, New York, 1969).
[8] C. E. Campbell, Phys. Lett. **44A**, 471 (1973).
[9] C. C. Chang and C. E. Campbell, Phys. Rev. B **15**, 4238 (1977).
[10] E. Krotscheck, Phys. Rev. B **33**, 3158 (1986).
[11] C. E. Campbell and E. Feenberg, Phys. Rev. **188**, 396 (1969).
[12] E. Krotscheck, Q.-X. Qian, and W. Kohn, Phys. Rev. B **31**, 4245 (1985).
[13] M. Saarela, Phys. Rev. B **33**, 4596 (1986).
[14] M. Saarela and J. Suominen, in *Condensed Matter Theories*, edited by J. S. Arponen, R. F. Bishop, and M. Manninen (Plenum, New York, 1988), Vol. 3, p. 157.
[15] M. Saarela and J. Suominen, in *Condensed Matter Theories*, edited by J. Keller (Plenum, New York, 1989), Vol. 4, p. 377.
[16] P. Kramer and M. Saraceno, *Geometry of the Time-Dependent Variational Principle in Quantum Mechanics, Lecture Notes in Physics*, Vol. 140 (Springer, Berlin, 1981).
[17] A. K. Kerman and S. E. Koonin, Ann. Phys. (N.Y.) **100**, 332 (1976).
[18] C. C. Chang and C. E. Campbell, Phys. Rev. B **13**, 3779 (1976).
[19] B. E. Clements, E. Krotscheck, J. A. Smith, and C. E. Campbell, Phys. Rev. B **47**, 5239 (1993).
[20] R. P. Feynman and M. Cohen, Phys. Rev. **102**, 1189 (1956).
[21] R. P. Feynman, Phys. Rev. **94**, 262 (1954).
[22] M. S. Wertheim, J. Math. Phys **8**, 927 (1967).
[23] E. Krotscheck and C. J. Tymczak, Phys. Rev. B **45**, 217 (1992).
[24] B. E. Clements, H. Forbert, E. Krotscheck, and M. Saarela, J. Low Temp. Phys. **95**, 849 (1994).
[25] L. Pozhar, K. E. Gubbins, and J. K. Percus, Phys. Rev. E **48**, 1819 (1993), and references therein.
[26] B. E. Clements, E. Krotscheck, and M. Saarela, Z. Phys. B **94**, 115 (1994).
[27] H. W. Jackson, Phys. Rev. A **4**, 2386 (1971).
[28] H. J. Lauter, H. Godfrin, V. L. P. Frank, and P. Leiderer, in *Excitations in Two-Dimensional and Three-Dimensional Quantum Fluids*, Vol. 257 of *NATO Advanced Study Institute, Series B: Physics*, edited by A. F. G. Wyatt and H. J. Lauter (Plenum, New York, 1991), p. 419.
[29] H. J. Lauter, H. Godfrin, V. L. P. Frank, and P. Leiderer, Phys. Rev. Lett. **68**, 2484 (1992).
[30] P. A. Crowell and J. D. Reppy, Phys. Rev. Lett. **70**, 3291 (1993).
[31] L. D. Landau and E. M. Lifshitz, *Statistical Physics, Course of Theoretical Physics*, Vol. V (Pergamon, London, 1958).
[32] G. Zimmerli, G. Mistura, and M. H. W. Chan, Phys. Rev. Lett. **68**, 60 (1992).
[33] D. S. Greywall and P. A. Busch, Phys. Rev. Lett. **67**, 3535 (1991).
[34] M. J. McKenna, T. B. Brosius, and J. D. Maynard, Phys. Rev. Lett. **69**, 3346 (1992).
[35] L. V. Hove, Phys. Rev. **95**, 249 (1954).
[36] J. Pitaevskii and S. Stringari, Phys. Rev. B **45**, 13133 (1992).
[37] J. Mathews and R. L. Walker, *Mathematical Methods of Physics*, 2nd ed. (Benjamin, New York, 1970), p. 131.
[38] R. A. Cowley and A. D. B. Woods, Can. J. Phys. **49**, 177 (1971).

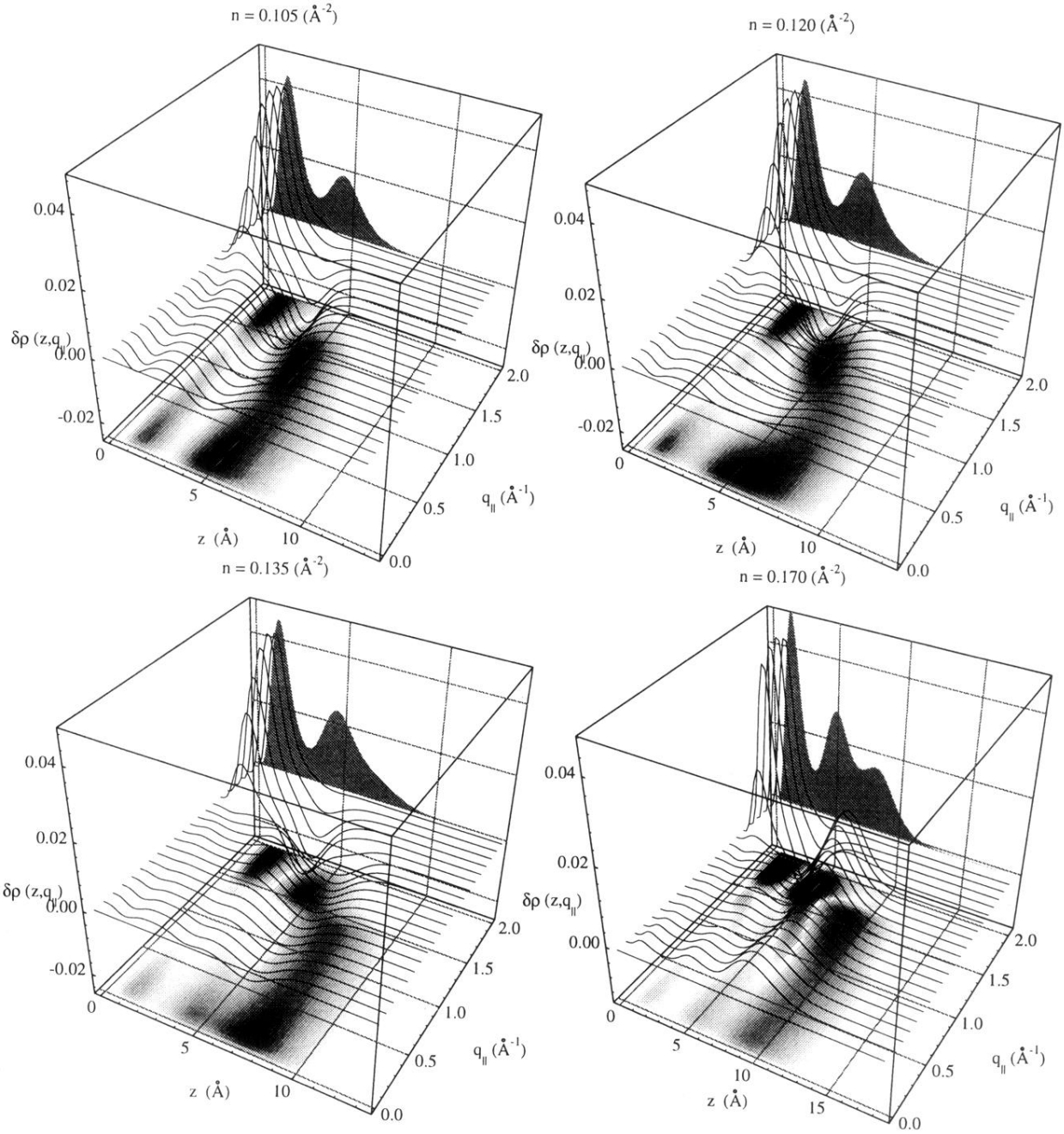

FIG. 10. Transition densities of the lowest excited state of a double layer films with coverages of $n = 0.105$ Å^{-2} (upper left), $n = 0.120$ Å^{-2} (upper right), $n = 0.135$ Å^{-2} (lower left), and a triple-layer films with $n = 0.170$ Å^{-2} (lower right). The shaded area in the background is the ground state profile, the grayscales at the bottom of the figure are a measure for the amplitude of $\delta\rho_1(z, q_\parallel)$.

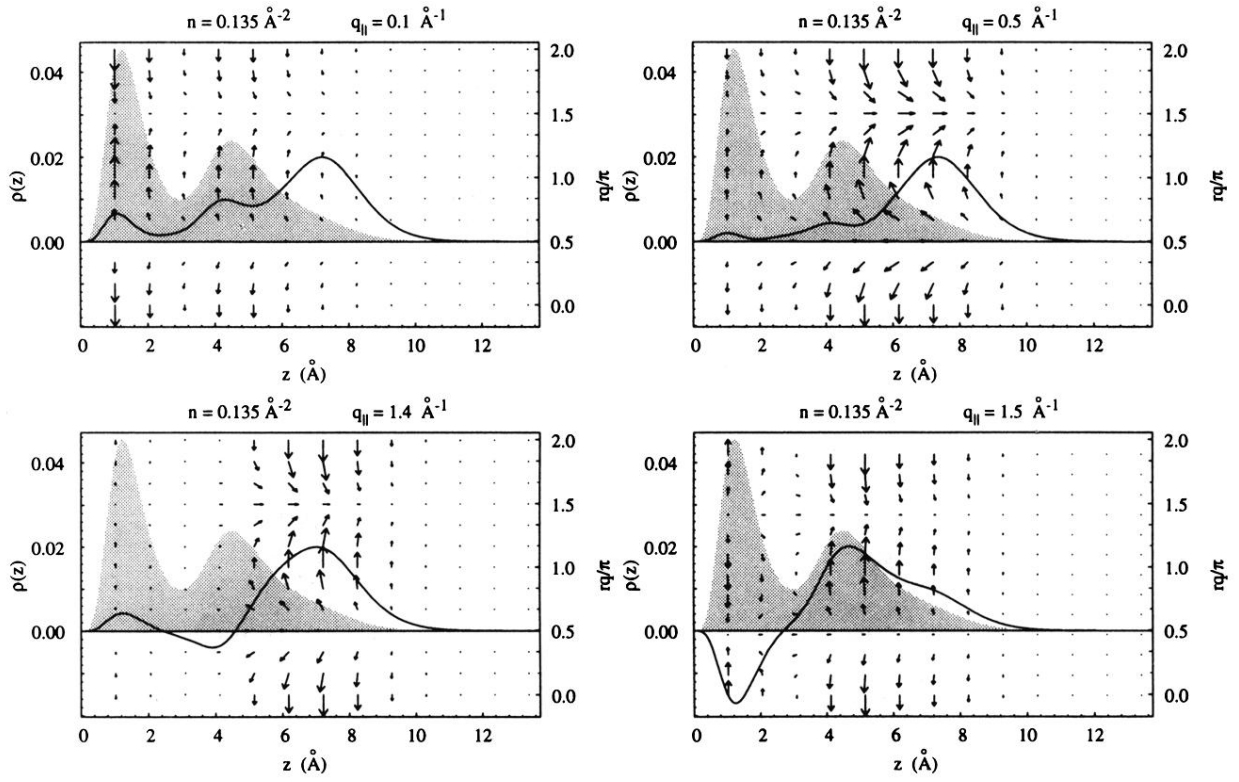

FIG. 11. Particle currents for the lowest excited state of a doublelayer film with a coverage of $n = 0.135$ Å^{-2}. See Fig. 8 for further explanations.

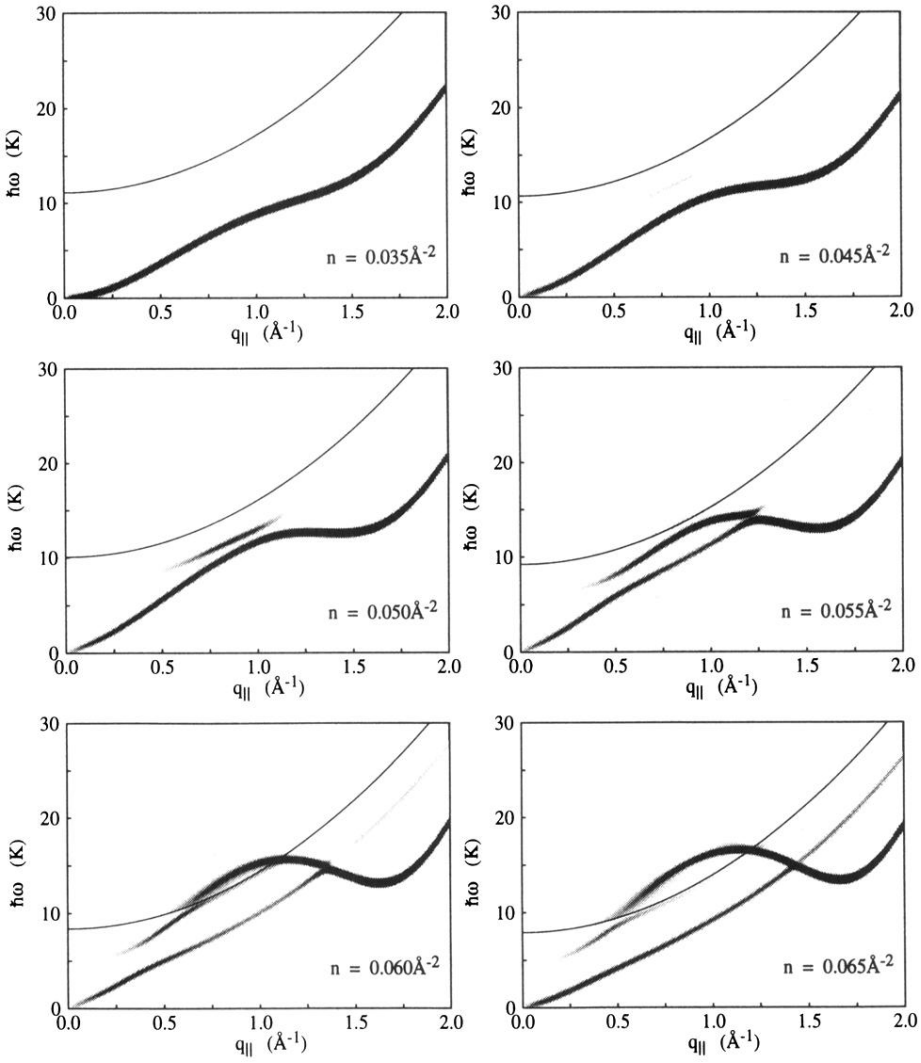

FIG. 12. The dynamic structure function $S(q_{\|}, \omega)$ is shown, in the Feynman approximation, for a representative sample of monolayer films. The grayscale indicates the strength of $S(q_{\|}, \omega)$, the parabolic line in the middle of the frames is the boundary of continuum states. All modes *below* this continuum are discrete in Feynman approximation; in order to display their relative strength we have artificially broadened these states by a Gaussian of approximately 0.5-K width.

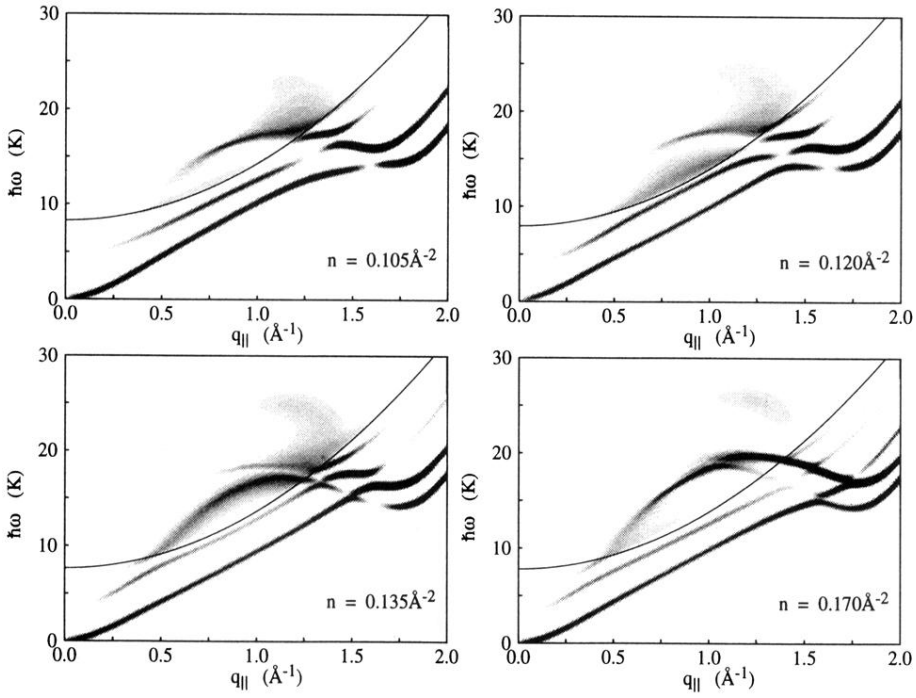

FIG. 13. Same as Fig. 12 for double- and triple-layer films for four different coverages.

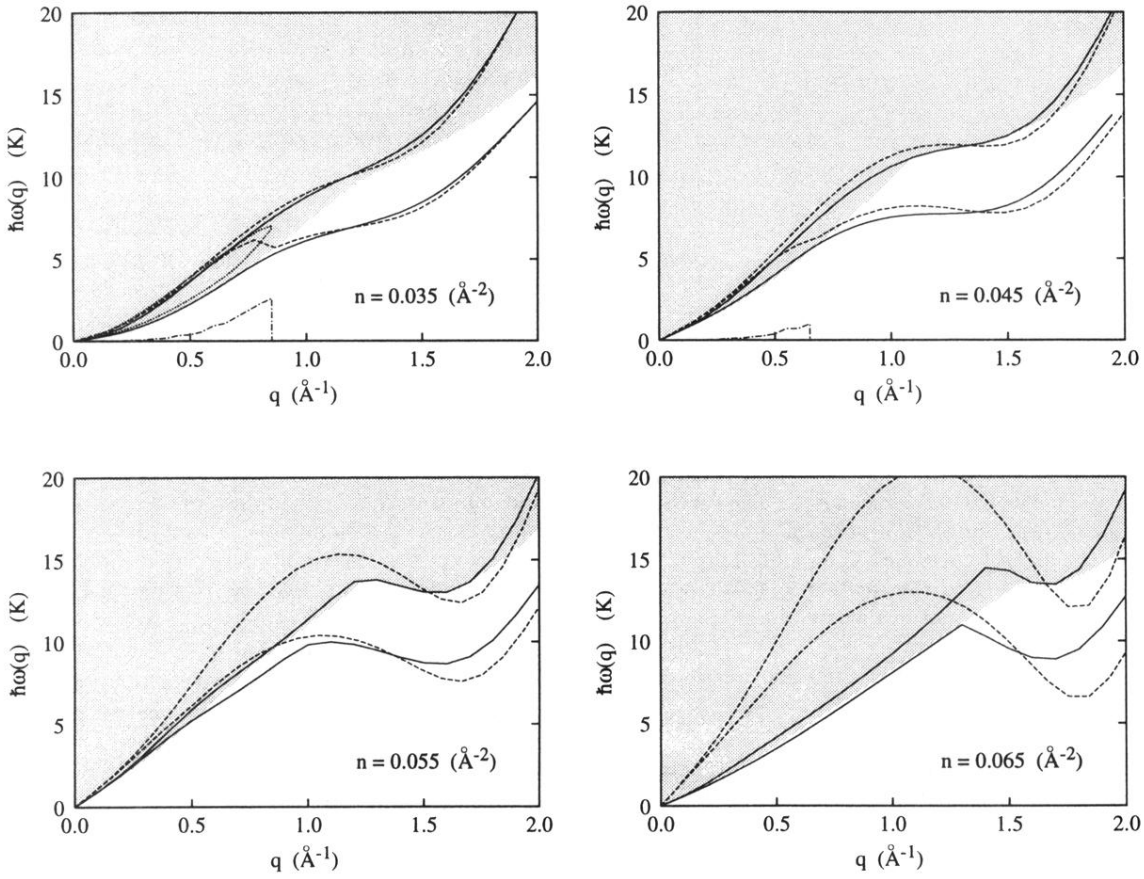

FIG. 5. Dispersion relation of the lowest excited state of monolayer films with coverages of $n = 0.035$, 0.045, 0.055, and 0.065 Å^{-2} (solid lines) and for two-dimensional ^{4}He at the same densities (dashed lines). The lower curves are the CBF-BW results, and the upper curves the results from the Feynman theory. The dash-dotted lines for $n = 0.035$ Å^{-2} and $n = 0.045$ Å^{-2} are the imaginary parts of modes lying slightly above $\omega_{\text{crit}}(q)$. These modes are shown, in the case $n = 0.035$ Å^{-2}, as a closed dotted line. The gray-shaded area is the regime of energies $\omega > \omega_{\text{crit}}(q)$ where the excitation energies become complex.

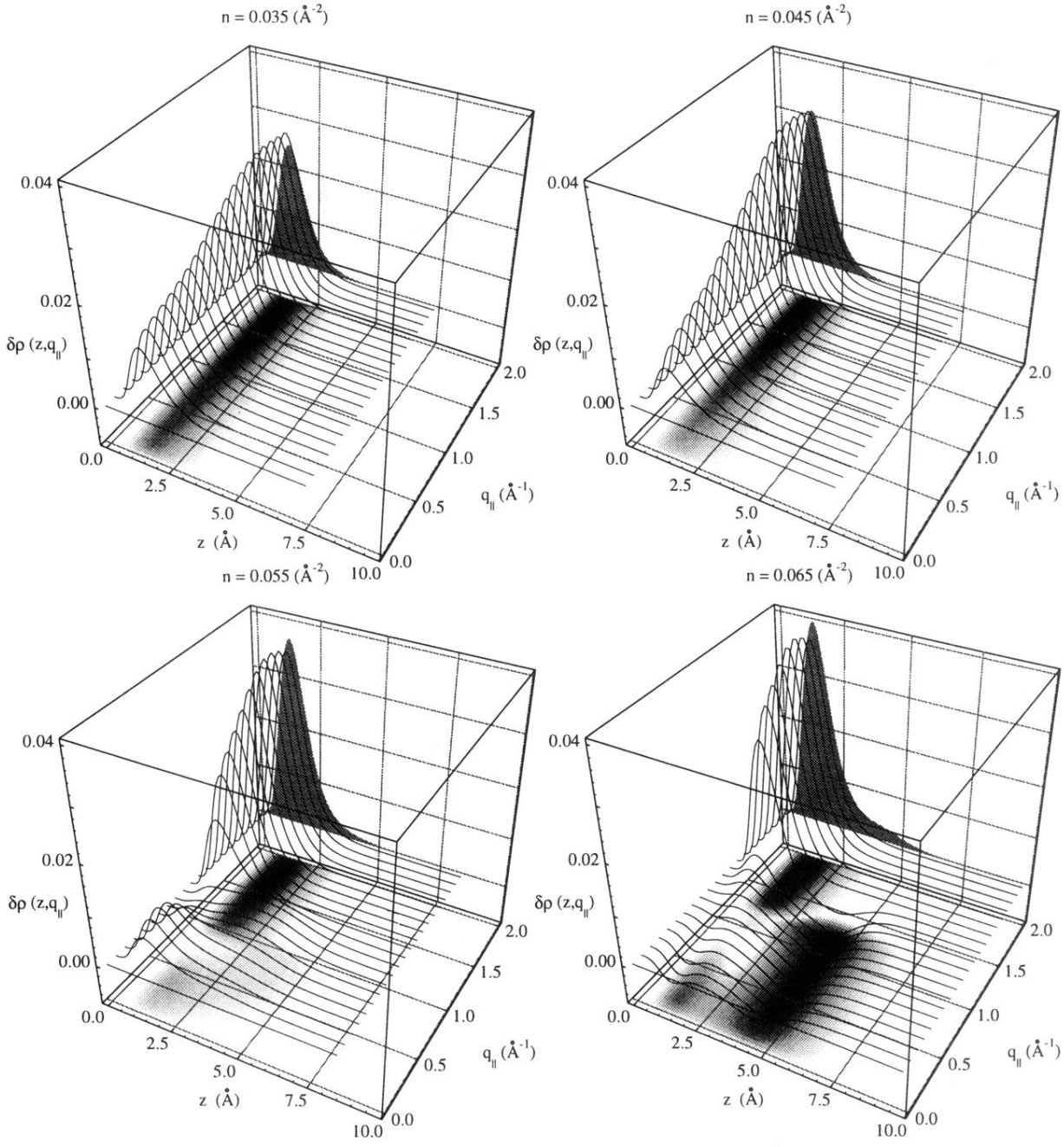

FIG. 6. Transition densities of the lowest excited state of monolayer films with coverages of $n = 0.035$ Å^{-2} (upper left), $n = 0.045$ Å^{-2} (upper right), $n = 0.055$ Å^{-2} (lower left) and $n = 0.065$ Å^{-2} (lower right). The shaded area in the background is the ground state profile, the grayscales at the bottom of the figure are a measure for the amplitude of $\delta\rho_1(z, q_{||})$.

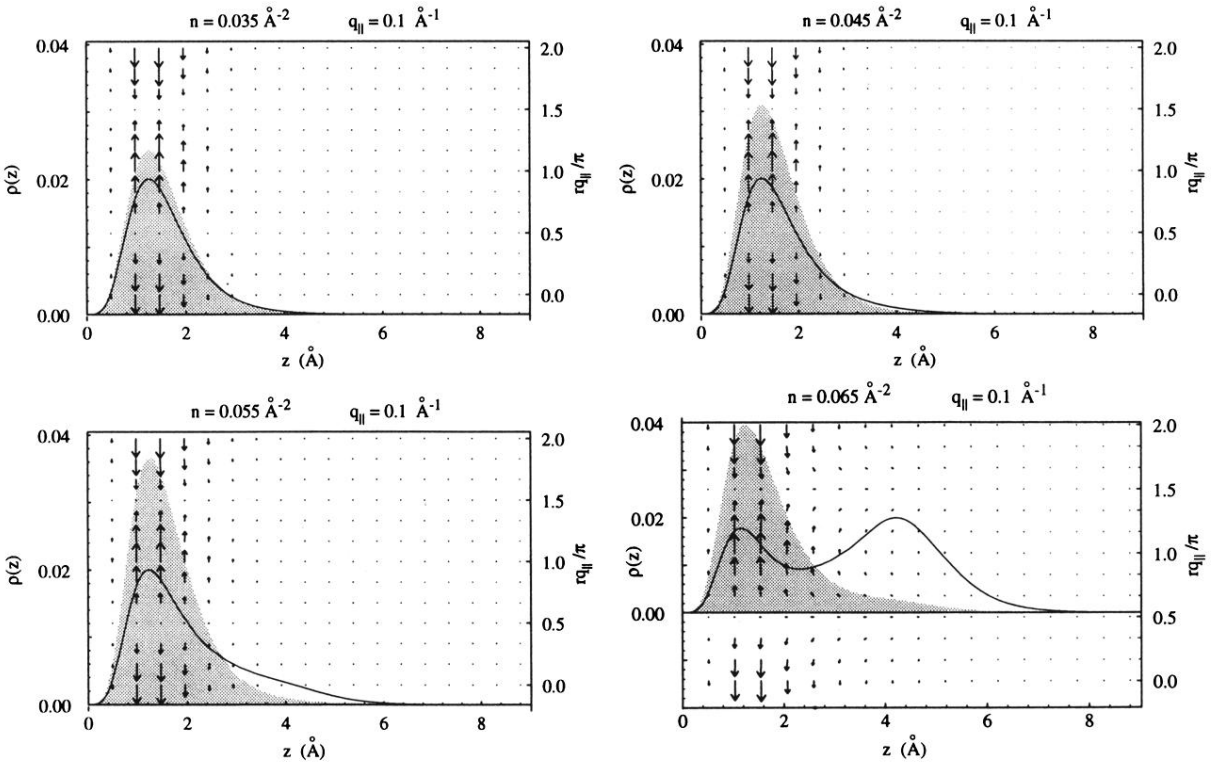

FIG. 7. The transition densities (solid lines) are shown for long-wavelength excitations $q_{\|} = 0.1$ Å^{-1} for four monolayer films with $n = 0.035$, 0.045, 0.055, and $n = 0.065$ Å^{-2}. The shaded area and the scale on the left side correspond to the background density. The vector fields superimposed to the figures show the particle currents corresponding to these excitations.

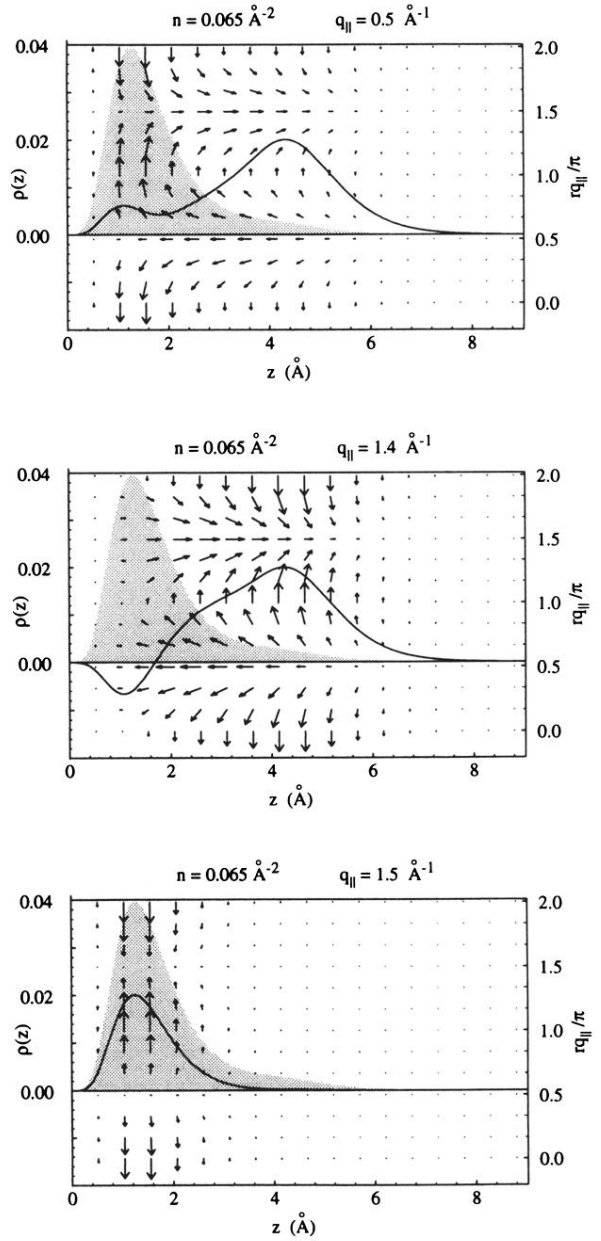

FIG. 8. Particle currents for the lowest excited state of a monolayer film with a coverage of $n = 0.065$ Å^{-2} and parallel momenta $q_{\|} = 0.5$ Å^{-1} (upper figure), $q_{\|} = 1.4$ Å^{-1} (middle figure) and , $q_{\|} = 1.5$ Å^{-1} (lower figure). The shaded area and the scale on the left side correspond to the background density, the solid line is the transition density.